---Division of New Materials Science----------

Incomplete Devil's Staircase in the Magnetization Curve of $SrCu_2(BO_3)_2$

Takigawa and Y. Ueda Groups

Magnetization plateaus in frustrated quantum spin systems are manifestation of Wigner crystallization of magnons, resulting from competition between the kinetic energy and repulsive interaction. The layered compound $SrCu_2(BO_3)_2$ has played a prominent role in this problem since the discovery of a sequence of plateaus at 1/8, 1/4, and 1/3 of the saturation magnetization. Recent experiments have revealed a rich phase diagram below the 1/4 plateau, but with controversial results. We have performed magnetic torque and ^{11}B-NMR measurements in high magnetic field up to 34 T at the Grenoble High Magnetic Field Laboratory and precisely determined the sequence and the spin structures of the plateaus [1].

The magnetization curve under static magnetic fields was accurately determined from the torque (τ) data (Fig. 1), which consist of two terms: $\tau = a\mathbf{M} \times \mathbf{H} + b(\mathbf{M}\bullet\nabla)\mathbf{M}$, the first one proportional to the transverse magnetization and the second one to the longitudinal magnetization. The first term can be eliminated by taking a linear combination of two measurements of τ/H taken at different sample positions with the requirement that the longitudinal magnetization is zero in the dimer singlet phase below 15 T. The longitudinal magnetization thus obtained clearly shows three plateaus at the ratio 1/8:2/15:1/6 below the 1/4 plateau and two intermediate phases below and above the 1/6 plateau.

The plateau phases are associated with symmetry breaking commensurate spin superstructures, which were determined from the ^{11}B-NMR spectrum (Fig. 2 (left)). We have established a systematic way to determine the spin structure from the NMR spectra and the results are displayed in Fig. 2 (right). All plateaus show stripe order of triplets. The structure of 1/6 (1/8) plateau can be obtained by removing every other triplet from the one of the 1/3 (1/4) plateaus. The 2/15 structure exhibits a sequence of domains of 1/8-1/8-1/8-1/6 structure, showing how the proliferation of domain walls leads to a structure of higher order commensurability. This suggests that the plateau sequence can be interpreted as a "devil's staircase", which is an infinite sequence of commensurate phases [2]. However, the NMR spectra in the intermediate phase consist of only broad lines, indicating that what is observed here is an example of "incomplete devil's staircase", in which the infinite sequence of high order commensurate phases with small steps are replaced by incommensurate phases [3].

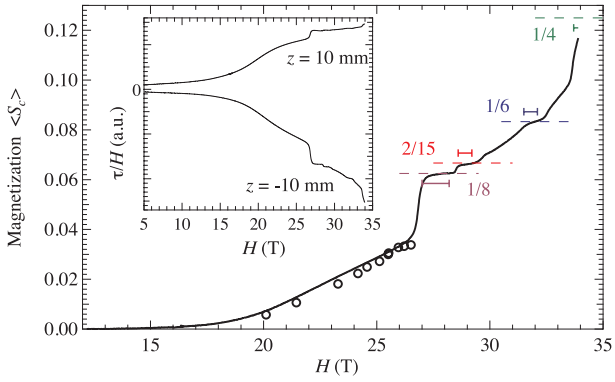

Fig. 1. Inset: The torque divided by field vs. field obtained at T=60 mK with the sample positioned at 10 mm off the nominal field center. Main panel: The thick black line represents the longitudinal magnetization with the vertical scale appropriately adjusted. The magnetization values at 1/8, 2/15, 1/6, and 1/4 of the saturation are shown by the dashed lines. The horizontal bars indicate the field range of the plateaus determined by NMR. The open circles show the magnetization determined from the Cu NMR shift data (Kodama *et al*., Science 298, (2002) 395).

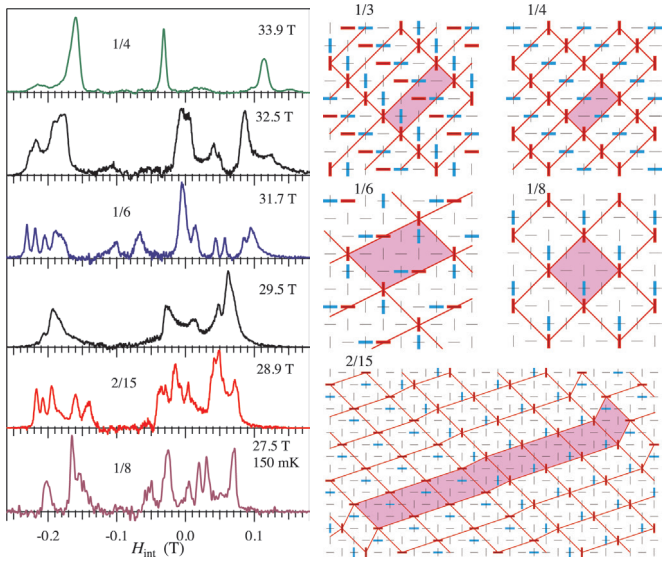

Fig. 2 . (left) The distribution of internal magnetic field at the ^{11}B nuclei obtained by deconvoluting the quadrupole splitting structure from the experimental NMR spectra obtained at T=430 mK unless explicitly indicated. (right) The spin superstructure of the plateaus phases. The thin black lines show the lattice of orthogonal Cu dimers in one layer. The thick red lines show the triplet dimers carrying the largest magnetization in the same layer while the blue lines indicate these triplets on the neighboring layers. The unit cell of each superstructure is shown by the shaded area.

References

[1] M. Takigawa, M. Horvatić, T. Waki, S. Krämer, C. Berthier, F. Lévy-Bertrand, I. Sheikin, H. Kageyama, Y. Ueda, and F. Mila, Phys. Rev. Lett. **110**, 067210 (2013).

[2] P. Bak, Rep. Prog. Phys. **45**, (1982) 587.

[3] S. Arby, *Solitons and Condensed Matter Physics*, edited by A. R. Bishop and T. Schneider (Springer-Verlag, Berlin, 1979), p. 264.

Authors

M. Takigawa, M. Horvatić, T. Waki, S. Krämer, C. Berthier, F. Lévy-Bertrand, I. Sheikin, H. Kageyama, Y. Ueda, and F. Mila

Hidden Multipole Order in Yb_2Pt_2Pb with the Orthogonal Dimer Structure

Sakakibara Group

When a Yb^{3+} ion ($4f^{13}$) is situated in a crystalline electric field of low symmetry, a Kramers doublet becomes the ground state of the J=7/2 multiplet. Magnetic properties of such systems can be usually described in terms of a magnetic *dipole* moment carried by the Kramers doublet. Here we show that the tetragonal compound Yb_2Pt_2Pb, which orders antiferromagnetically at T_N=2.1 K [1], exhibits a very unusual ordered state in a magnetic field, whose order parameter is likely to be a high-rank magnetic *multipole* moment [2].

The Yb lattice in Yb_2Pt_2Pb can be viewed as being composed of orthogonal dimers aligned along [110] or [1-10] directions [1]; we can define two sublattices of Yb ions: sublattice A of [110] dimers and sublattice B of [1-10] dimers. In the preceding experiment, Ochiai *et al*. [3] have shown that the Yb moment has a strong Ising anisotropy along the dimer axis. When a magnetic field H is applied parallel to [110], the antiferromagnetic moments on the sublattice B are decoupled from H because their Ising axes are perpendicular to H. Accordingly, only the moments on sublattice A respond to H and the phase diagram is given in Fig. 1a, where three different ordered phases I, II' and III exist. The magnetic structures of phases I and III are shown in Figs. 2a and 2c, respectively. In phase I, both sublattices A and B are essentially in a collinear structure. In phase III, magnetic moments on sublattice B remain in a collinear structure but those on sublattice A become paramagnetic. Ochiai *et al*. [3] pointed out that the highly anisotropic magnetic properties can be understood by assuming the ground state doublet of Yb^{3+} ion to be predominantly composed of states $|\pm 7/2\rangle$ with the local quantization axis parallel to either [110] or [1-10].

There is another phase, phase II', in the phase diagram

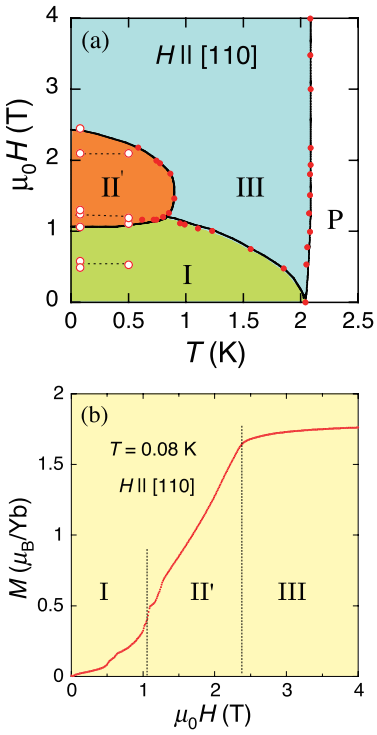

Fig. 1. (a) Magnetic phase diagram of Yb_2Pt_2Pb for $H \parallel [110]$. (b) Field variation of the magnetization of Yb_2Pt_2Pb for $H \parallel [110]$ measured at 80 mK.

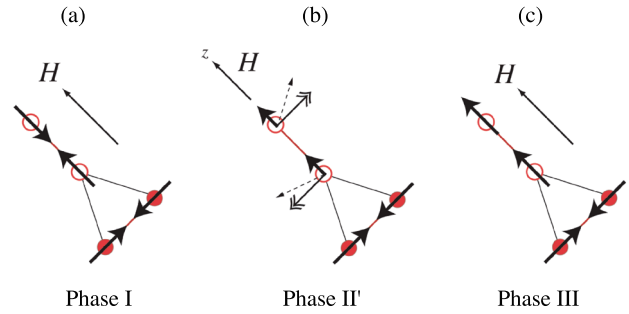

Fig. 2. Proposed magnetic structures of Yb_2Pt_2Pb for $H \parallel [110]$. (a) Phase I. Each Yb sublattice has a collinear structure. Thick arrows indicate the Yb magnetic moment. (b) Phase II'. Sublattice B (solid circles) remains in a collinear state, whereas sublattice A (open circles) exhibits a pseudo-spin flop. Dashed arrows denote the pseudo spins whereas double arrows indicate the multipole moments. (c) Phase III. Sublattice B remains in a collinear state, whereas sublattice A becomes parmagnetic.

[3]. The exact nature of phase II', however, has not been clear in the preceding experiments. We have examined the low temperature magnetization of Yb_2Pt_2Pb and found that the Yb magnetic moment increases almost linearly in phase II' and saturates without discontinuity; quite unexpectedly, the II'-III transition is of second order. This behavior of phase II' is apparently incompatible with the Ising anisotropy of the Yb moment. We propose that a high-rank magnetic multipole moment is the order parameter in phase II'. For simplicity, let us assume the wave functions of the Kramers doublet to be $|\pm 7/2\rangle$. In a pseudo-spin representation, the z component is the magnetic dipole J_z. On the other hand, the x and y components are rank-7 magnetic multipoles (*octacosahectapoles*). It can then be shown that a pseudo-spin flop occurs in a magnetic field along the Ising axis, if an interaction between the multipole moments is sufficiently strong (Fig.2 b) [2]. In this situation, the magnetic moment along [110] linearly increases with H and continuously saturates, as observed by experiment.

References

[1] M. S. Kim, M. C. Bennett, and M. C. Aronson, Phys. Rev. B **77**, 144425 (2008).
[2] Y. Shimura, T. Sakakibara, K. Iwasawa, K. Sugiyama, and Y. Onuki, J. Phys. Soc. Jpn. **81**, 103601 (2012).
[3] A. Ochiai, S. Matsuda, Y. Ikeda, Y. Shimizu, S. Toyoshima, H. Aoki, and K. Katoh, J. Phys. Soc. Jpn. **80**, 123705 (2011).

Authors

Y. Shimura, T. Sakakibara, K. Iwasawa[a], K. Sugiyama[a], and Y. Onuki[a]
[a]Osaka University

Hydrogen Bond-promoted Metallic State in a Purely Organic Single-component Conductor

Mori Group

Realization of "purely organic single-component molecular metals" has been one of the long-standing open problems in chemistry, physics, and materials science. As is well known, purely organic materials are normally insulating. Recently, Mori group unveils a new type of purely organic single-component molecular conductors based on a catechol-fused ethylenedithiotetrathiafulvalene, H_2Cat-EDT-TTF, and its diselena analogue, H_2Cat-EDT-ST, which are designed and synthesized by us [1]. These conductors are the unprecedented single component systems composed of molecular units, H_3(Cat-EDT-TTF)$_2$ and H_3(Cat-EDT-ST)$_2$,

with the highly symmetric intra-unit hydrogen bond. Their electrical conductivity at room temperature is significantly higher than that for the previously reported purely organic single-component systems. Under the moderate physical pressure, moreover, the metallic behavior appeared in the temperature dependence of the electrical resistivity. The higher electrical conductivity observed in our systems is attributed to the hydrogen bond-promoted delocalization of charge carriers, which are generated through the partial oxidation of the H_2Cat-EDT-TTF and H_2Cat-EDT-ST molecules [2].

A new type of purely organic single component molecular conductors, κ-H_3(Cat-EDT-TTF)$_2$ and κ-H_3(Cat-EDT-ST)$_2$, hereinafter described as κ-S and κ-Se, respectively, were obtained as black plate-like crystals by electrochemical oxidation of the corresponding donor molecules, H_2Cat-EDT-TTF and H_2Cat-EDT-ST, in the presence of the base, 2,2'-bipyridine. The minimal molecular unit, the H_3(Cat-EDT-TTF)$_2$ composition (Fig. 1), is established by the formation of an intra-unit hydrogen bond, O..H..O, between the catechol moieties of the donor molecules, where the one hydroxyl proton is deprotonated. The oxygen–oxygen distance in the hydrogen bond, d(O..O), is 2.486(5) Å and 2.509(8) Å at room temperature, and 2.453(5) Å and 2.443(8) Å at 50 K and 30 K for κ-S and κ-Se, respectively, which are much shorter than the length of the normal O–H..O type hydrogen bond, d(O..O) 2.7 ~ 3.0 Å. Because of this strong hydrogen bonding nature, the bonded hydrogen atom is nearly located at the center between two oxygen atoms, in contrast to the asymmetric hydrogen distribution in the normal hydrogen bonds. The minimal molecular units are assembled into the purely organic single component crystal.

The electrical conductivity at room temperature is significantly high, 3.5 and 19 S cm^{-1} for κ-S and κ-Se, respectively. These values are one or two orders of magnitude higher than the highest reported value, σ_{rt} = 10^{-1} S cm^{-1}, in the purely organic single-component systems, to our best knowledge. As temperature is decreased, the electrical resistivity of these systems exponentially increases with the energy gap Δ/k_B, of 2400 K for κ-S and 1200 K for κ-Se, respectively. The physical pressure is a good tool to change the electronic states by the modulation of the intermolecular interactions. We observed dramatic changes in the temperature variation in the electrical resistivity under pressure for κ-Se. Under the pressure above 1.3 GPa, the electrical resistivity monotonically decreases with reducing temperature down to around 150 K, in striking contrast with the semiconducting behavior at ambient pressure, although the resistive curve turns to increase at low temperature. Thus, the metallic states emerge with the simultaneous suppression of the semiconducting energy gap by the application of the pressure of only 1 GPa. To our knowledge, this is the lowest metallization pressure among the purely organic single-component systems.

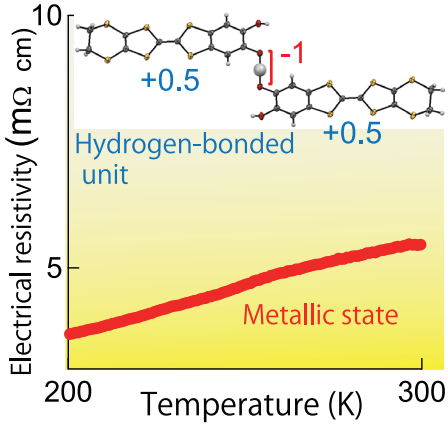

Fig. 1. Structure of the molecular unit and the metallic state in the purely organic single-component conductor. The "purely organic single-component conductor" developed by Mori's group with the world record conductivity at room temperature (19 Scm^{-1}) is composed of the electrically neutral and symmetric molecular units, where the charge is widely delocalized. The assembled units construct the two-dimensional conducting layers which afford the metallic state under the lowest pressure of around 1 GPa.

Our system demonstrates that the symmetric hydrogen bond constructs the new type of the purely organic single-component molecular conductors which are composed of highly symmetric molecular units. Moreover, we found that the formation of the symmetric hydrogen bond promoted the intermolecular delocalization of the generated carriers, associated with the enhancement of the electrical conductivity. We believe that our new type of molecular conductors with the symmetric intra-unit hydrogen bond will realize the first purely organic single-component molecular metal at ambient pressure. A tetraselenafulvalene (TSF)-type analogue, in which all the sulfur atoms in the TTF part of the present system are replaced with selenium atoms, is a promising candidate for the ambient-pressure metal, because the further enhanced intermolecular interactions are expected.

References
[1] H. Kamo, A. Ueda, T. Isono, K. Takahashi, and H. Mori, Tetrahedron Lett. **53**, 4385 (2012).
[2] T. Isono, H. Kamo, A. Ueda, K. Takahashi, A. Nakao, R. Kumai, H. Nakao, K. Kobayashi, Y. Murakami, and H. Mori, Nature Commun. **4**, 1344 (2013).

Authors
T. Isono, H. Kamo, A. Ueda, K. Takahashi[a], A. Nakao[b], R. Kumai[c], H. Nakao[c], K. Kobayashi[c], Y. Murakami[c], and H. Mori
[a]Kobe University
[b]Research Center for Neutron Science and Technology, CROSS
[c]Institute of Materials Structure Science, KEK

Quantum Monopolar Fluctuations in the Exchange-based Spin Ice System $Pr_2Zr_2O_7$

Nakatsuji Group

Spin ice is a magnetic analogue of H_2O ice that harbors dense static disorder. Dipolar interactions between classical Ising spins on pyrochlore lattice yield a frozen frustrated state with residual configurational Pauling entropy [1]. Mimicking the formation of an H_3O^+–OH^- electric dipole in water ice, a spin flip from the spin ice manifold fractionalizes into a pair of emergent magnetic monopolar quasiparticles with Coulomb attraction. In classical spin ice, monopole dynamics is diffusive –only activated thermally or by external magnetic field. The classical nature of Ising spins precludes attainment of thermal equilibrium at temperatures below the effective nearest neighbor energy scale J_{ff}. Introducing quantum fluctuations is of great interest as it enhances dynamics and might allow coherent propagation of magnetic charge (Fig. 1), much as spinons in one dimensional quantum magnets.

Here, we report the experimental observation of spin ice correlations and quantum dynamics in a new class of spin ice based on exchange interactions, $Pr_2Zr_2O_7$ [3]. We have succeeded in growing high quality single crystals at ISSP, which are stoichiometric to the 1-2% level. Inelastic

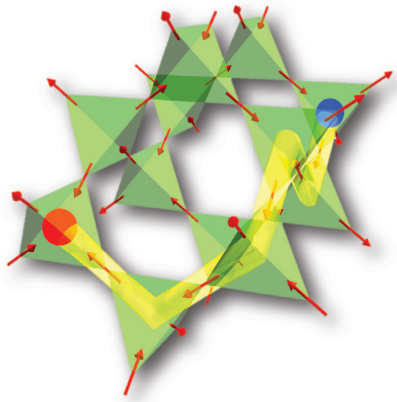

Fig. 1. Schematic illustration of magnetic monopolar quasi-particle with quantum dynamics. Red arrows denote magnetic moment. Red and Blue spheres indicate a pair of magnetic monopoles.

neutron scattering measurements revealed that the crystalline electric field (CEF) ground state of Pr^{3+} is magnetic doublet with <111> Ising anisotropy, as in classical spin ice systems. AC-magnetic susceptibility and specific heat data show activated dynamics and residual entropy below 0.1 K, again similar to the behavior in classical spin ice systems. However, Curie-Weiss behavior in the temperature dependence of magnetic susceptibility for $T < 10$ K indicated an effective moment $\mu_{\rm eff} = 2.5(1)\mu_{\rm B}$ that is four times smaller than for dipolar spin ice $Dy_2Ti_2O_7$ where $\mu_{\rm eff} = 10\mu_{\rm B}$. Correspondingly, $Pr_2Zr_2O_7$ displays an antiferromagnetic (AFM) Weiss temperature $\theta_{\rm CW} = -1.4(1)$ K compared to the ferromagnetic (FM) $\theta_{\rm CW} \approx +0.5$ K for dipolar $Dy_2Ti_2O_7$.

Quasi-static spin correlations were investigated using elastic neutron scattering and the result at $T = 0.1$ K is shown in Fig. 2(a). Sharp pinch point features near (111) and particularly (002), bear evidence of a divergence free two-in two-out spin configuration on each tetrahedron. Indeed, the elastic Q-map resembles a classical Monte Carlo simulation for an exchange only model, which indicates dominant FM superexchange interactions in $Pr_2Zr_2O_7$. $\theta_{\rm CW}$ is however, negative and this suggests the exchange Hamiltonian includes AFM transverse terms that induce quantum dynamics. Figure 2(b) shows the Q-map of *inelastic* scattering at $\hbar\omega = 0.25$ meV and $T = 0.1$ K. While the overall

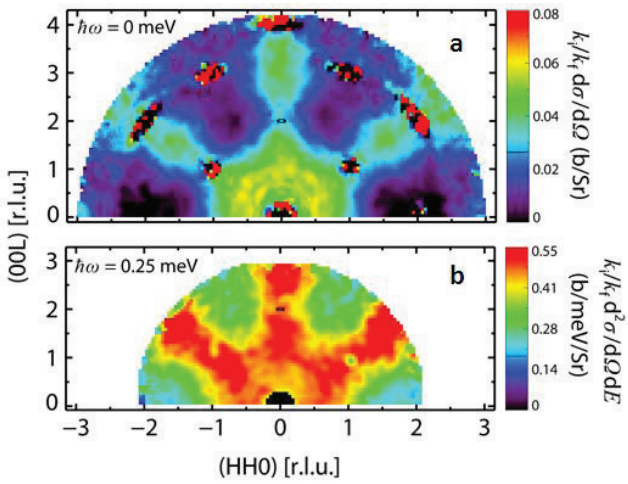

Fig. 2. Spin ice correlations and quantum dynamics in $Pr_2Zr_2O_7$ probed through elastic and inelastic neutron scattering. (a) Elastic Q-map at 0.1 K with pinch points at (002), (111), and (-1-11). 22 K data was subtracted as a high-temperature background to cancel elastic nuclear scattering processes at Bragg peak. (b) Inelastic Q-map at $\hbar\omega = 0.25$ meV and $T = 0.1$ K after subtracting the corresponding data at 15 K as background [3].

pattern resembles the nominally elastic scattering (Fig. 2a), the pinch points have vanished. Excited states thus differ from the ground state by the appearance of tetrahedra that violate the ice rule or in other words by the presence of magnetic monopoles, furnishing evidence for magnetic monopolar quantum fluctuations. Such inelastic scattering accounts for >90% of the magnetic scattering cross section at 0.1 K, showing that magnetism in $Pr_2Zr_2O_7$ is dominated by quantum fluctuations. Our observation in $Pr_2Zr_2O_7$ is unlike any previously documented in an insulating crystalline magnet. The interplay between monopolar quantum dynamics and itinerant electrons may play an important role in the isostructural Kondo lattice system $Pr_2Ir_2O_7$ [4].

References

[1] S. T. Bramwell and M. J. P. Gingras, Science **294**, 1495 (2001).
[2] C. Castelnovo, R. Moessner, and S. L. Sondhi, Nature **451**, 42 (2008).
[3] K. Kimura, S. Nakatsuji, J.-J. Wen, C. Broholm, M. B. Stone, E. Nishibori, and H. Sawa, to be published in Nature Communications (2013).
[4] Y. Machida, S. Nakatsuji, S. Onoda, T. Tayama, and T. Sakakibara, Nature **463**, 210 (2010).

Authors

K. Kimura, S. Nakatsuji, J.-J. Wen[a], C. Broholm[a,b,c], M. B. Stone[c], E. Nishibori[d], and H. Sawa[d],
[a]Johns Hopkins University, USA
[b]National Institute of Standards and Technology, USA
[c]Oak Ridge National Laboratory, USA
[d]Nagoya University

Heavy Fermion Superconductivity in the Ferroquadrupolar State in the Quadrupolar Kondo Lattice $PrTi_2Al_{20}$

Nakatsuji Group

Orbital degree of freedom provides a various interesting phenomena such as colossal magnetoresistance, orbital ordering, and quantum spin-orbital liquid states. Although orbital degree of freedom strongly couples to spin and charge degrees of freedom in *d*-electron systems, *f*-electron systems with $4f^2$ configuration, such as cubic Pr and U based compounds, sometimes exhibit nonmagnetic ground state with a pure orbital degree of freedom known as quadrupole moments. In analogy with magnetic Kondo lattice systems, two competing interactions, RKKY type intersite coupling and quadrupolar Kondo effect, can be induced in *quadrupolar Kondo lattice systems* due to hybridization between 4*f* quadrupole and conduction(*c*-) electrons, which may lead to novel quantum criticality of quadrupole order.

Recently, we revealed that $PrTr_2Al_{20}$ (*Tr* = transition metal) is the first ideal quadrupolar Kondo lattice system that allows us to tune the hybridization strength and the quadrupolar ordering temperature [1]. Among them, $PrTi_2Al_{20}$ is the best studied and established to have nonmagnetic Γ_3 crystal electric field ground doublet with ferroquadrupolar ordering at $T_{\rm Q} = 2.0$ K [1-4] as well as strong *c-f* hybridization [1, 5].

Here, we report the heavy fermion superconductivity at $T_{\rm c} = 0.2$ K in the ferroquadrupolar ordered state of $PrTi_2Al_{20}$. The temperature dependence of critical field $B_{\rm c2}$ and weak differential paramagnetic effect indicate type-II superconductivity. Estimated effective mass m^* from $B_{\rm c2}$ and Sommerfeld coefficient γ is ~16 m_0, indicating moderately enhanced m^* by hybridization. The positive $\partial^2 B_{\rm c2}/\partial T^2$ at ~$T_{\rm c}$ and sensitivity of $T_{\rm c}$ to sample quality suggest the multi-gap

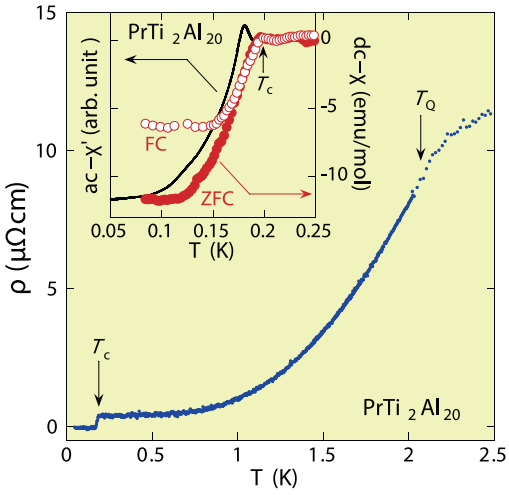

Fig. 1. Temperature dependence of the resistivity below 2.5 K in $PrTi_2Al_{20}$ (solid circle). Arrows indicate the ferro-quadrupole transition temperature T_Q = 2.0 K and superconducting transition temperature T_c = 0.2 K. Inset: T dependence of the real part of the ac-susceptibility (solid line) and dc-susceptibility for zero field cooled (ZFC, solid circle) and field cooled (FC, open circle).

nature of the superconductivity. These features provide an interesting counterpart to the superconductivity at T_c = 50 mK in the antiferro-quadrupole ordered state of $PrIr_2Zn_{20}$ [7, 8], where in contrast 4*f* electrons are well localized. More enhanced T_c and B_{c2} in $PrTi_2Al_{20}$ should come from the mass enhancement due to the strong hybridization between 4*f* and *c*-electrons.

References

[1] A. Sakai and S. Nakatsuji, J. Phys. Soc. Jpn. **80**, 063701 (2011).
[2] T. J. Sato, S. Ibuka, Y. Nambu, T. Yamazaki, A. Sakai, and S. Nakatsuji, arXiv0301828.
[3] T U. Ito, W. Higemoto, K. Ninomiya, H. Luetkens, C. Baines, A. Sakai, and S. Nakatsuji, J. Phys. Soc Jpn. **80**, 113703 (2011).
[4] M. Koseki, Y. Nakanishi, K. Deto, G. Koseki, R. Kashiwazaki, F. Shichinomiya, M. Nakamura, M. Yoshizawa, A. Sakai, and S. Nakatsuji, J. Phys. Soc. Jpn. **80**, SA049 (2011).
[5] M. Matsunami, M. Taguchi, A. Chainani, R. Eguchi, M. Oura, A. Sakai, S. Nakatsuji, and S. Shin, Phys. Rev. B **84**, 193101 (2011).
[6] A. Sakai, K. Kuga, and S. Nakatsuji, J. Phys. Soc. Jpn. **81**, 083702 (2012).
[7] T. Onimaru, K. T. Matsumoto, Y. F. Inoue, K. Umeo, Y. Saiga, Y. Matsushita, R. Tamura, K. Nishimoto, I. Ishii, T. Suzuki, and T. Takabatake, J. Phys. Soc. Jpn. **79**, 033704 (2010).
[8] T. Onimaru, K. T. Matsumoto, Y. F. Inoue, K. Umeo, T. Sakakibara, Y. Karaki, M. Kubota, and T. Takabatake: Phys. Rev. Lett. **106**, 197201 (2011).

Authors

A. Sakai, K. Kuga, and S. Nakatsuji

Evolution of *c*-*f* Hybridization and Two Component Hall Effect in β-$YbAlB_4$

Nakatsuji Group

Several recent studies of the mixed-valence compound β-$YbAlB_4$ have revealed the remarkable properties which are seemingly contradictory to one another within a conventional understanding of *f*-electron intermetallics. β-$YbAlB_4$ is the first Yb-based material in which highly renormalized electronic quasiparticles (with effective masses > 100 times larger than the bare electronic mass) superconduct [1, 2]. In addition, β-$YbAlB_4$ was found to have a quantum critical point at exactly zero magnetic field and zero pressure [3], suggesting the vanishing of an energy scale associated with an ordered electronic state, such as magnetism. On the other hand, in apparent contradiction to these low temperature properties, the Yb *f*-moment in β-$YbAlB_4$ shows strong valence fluctuations [4] (the Yb valence is +2.75) and has a high Kondo temperature (T_K ~ 200 - 300 K) [1, 3]; behaviors that usually lead to a Fermi liquid ground state with weakly renormalized quasiparticles. A study of the Hall effect sheds new light on the evolution of the electronic structure of β-$YbAlB_4$ and suggests how these behaviors can coexist [5].

The Hall effect measurements using high quality crystals of β-$YbAlB_4$ found that the Hall coefficient has strong temperature dependence and a minimum at T = 40 K (see Fig. 1), that bears a close similarity to Kondo rather than mixed-valence systems. The usual interpretation of this result would put the Kondo temperature at 40 K rather than 200 - 300 K, as was measured by the longitudinal resistivity. To answer the question of how β-$YbAlB_4$ can appear to have two Kondo temperatures separated by almost an order of magnitude, we suggested a two component Hall effect, which was supported by the magnetic field dependence of the Hall resistivity.

As the temperature is lowered below 100 K the Hall resistivity becomes non-linear; a careful analysis showed that the field dependence can be explained by the material having two field independent Hall coefficients, the combination of which leads to a non-linear Hall resistivity. Furthermore, this analysis allowed us to show that the mobility of the material strongly increases approaching the minimum at 40 K; thus demonstrating that the minimum in the Hall coefficient is indeed due to the onset of coherent transport in a second component of the electronic transport that has just 10% of the total carrier density.

The reason that these two components have such different Kondo temperatures is suggested by the Fermi surface of β-$YbAlB_4$ together with a recent theoretical analysis showing that the hybridization between conduction electrons and *f*-moments may vanish at certain points in momentum space [6]. These nodal points lead to a large difference in hybridization strength and thereby a different Kondo temperature between the two Fermi surfaces, one of which passes close to the nodal region and the other of which is well separated.

These results therefore suggest that the emergent second component arises from the Fermi surface that lies close to the region of vanishing hybridization that may be responsible for the quantum critical and superconducting behavior observed at low temperature. This scenario is consistent with a recent

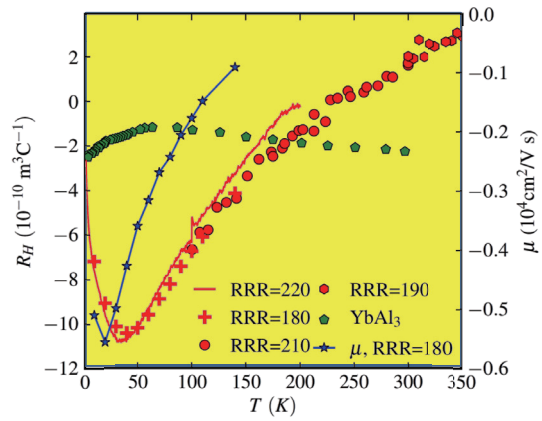

Fig. 1. The Hall coefficient (R_H) of β-$YbAlB_4$ vs temperature (T) for several different quality samples compared to a mixed valent compound $YbAl_3$ (left-hand axis). β-$YbAlB_4$ shows a strong temperature dependence characteristic for materials with incoherent skew-scattering from localized moments as expected when the Kondo interaction dominates. The Hall mobility μ obtained from the two band analysis is also shown (right-hand axis).

theoretical work which provides a phenomenological model for quantum criticality in β-$YbAlB_4$ [6].

References

[1] S. Nakatsuji, K. Kuga, Y. Machida, T. Tayama, T. Sakakibara, Y. Karaki, H. Ishimoto, S. Yonezawa, Y. Maeno, E. Pearson, G. G. Lonzarich, L. Balicas, H. Lee, and Z. Fisk, Nature Physics **4**, 603 (2008).
[2] K. Kuga, Y. Karaki, Y. Matsumoto, Y. Machida, and S. Nakatsuji, Phys. Rev. Lett. **101**, 137004 (2008).
[3] Y. Matsumoto, S. Nakatsuji, K. Kuga, Y. Karaki, N. Horie, Y. Shimura, T. Sakakibara, A. H. Nevidomskyy, and P. Coleman, Science **331**, 316 (2011).
[4] M. Okawa, M. Matsunami, K. Ishizaka, R. Eguchi, M. Taguchi, A. Chainani, Y. Takata, M. Yabashi, K. Tamasaku, Y. Nishino, T. Ishikawa, K. Kuga, N. Horie, S. Nakatsuji, and S. Shin, Phys. Rev. Lett. **104**, 247201 (2010).
[5] E. C. T. O'Farrell, Y. Matsumoto, and S. Nakatsuji, Phys. Rev. Lett. **109**, 176405 (2012).
[6] A. Ramires, P. Coleman, A. H. Nevidomskyy, and A. M. Tsvelik, Phys. Rev. Lett. **109**, 176404 (2012).

Authors

E. C. T. O'Farrell, Y. Matsumoto, and S. Nakatsuji

Quantum Compass Model Realized in Post-Perovskite Iridate $CaIrO_3$

Ohgushi Group

There is a new trend toward exploring Mott physics in 5*d* transition metal oxides with a strong spin-orbit interaction. Theoretical calculations on the Hubbard model revealed that the spin-orbit interaction drives a transition from a correlated metal to an insulator [1]. This novel Mott insulating state is actually realized in a layered perovskite Sr_2IrO_4, including Ir^{4+} ions with a $(t_{2g})^5$ electronic configuration [2]. In this compound, one hole among t_{2g} manifolds takes a complex wavefunction with the spin and orbital magnetic moments of 1/3 and 2/3 μ_B, respectively, and this state is now called the J_{eff} =1/2 state. The superexchange interaction across two Ir^{4+} ions in the J_{eff} =1/2 state is theoretically shown to be unique [3]. Whereas an antiferromagnetic Heisenberg interaction $J_1\mathbf{S}_i\cdot\mathbf{S}_j$ is dominant in a corner-shared IrO_6 bond, the magnetic interaction of the edge-shared IrO_6 bond becomes a highly anisotropic and ferromagnetic one, $-J_2S_i^zS_j^z$, where the *z* direction is perpendicular to the plane expanded by the two Ir atoms and two O atoms responsible for the edge-shared bond. This interaction, which is called the quantum compass model, captures great interests since a quantum spin liquid is realized when this interaction works on the honeycomb lattice (Kitaev model). To test the validity of this theory, it is necessary to elucidate the magnetic structure of an Ir oxide with an edge-sharing octahedral network.

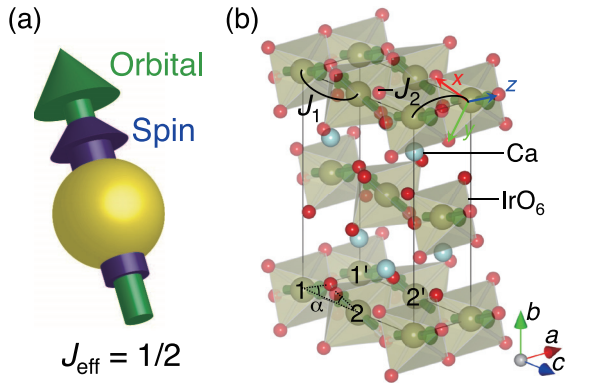

Fig. 1. (a) The schematic view of J_{eff} =1/2 state. (b) Magnetic structure of the post-perovskite $CaIrO_3$. The solid lines indicate the conventional unit cell, which is twice as large as the primitive unit cell. The magnetic interaction are also shown.

We performed resonant x-ray diffraction experiments at the *L* absorption edges for the post-perovskite-type compound $CaIrO_3$, which shows a Mott insulating behavior characterized by the charge gap ~0.17 eV and undergoes a transition to a canted antiferromagnetic state at 115 K [4]. By observing the magnetic signals, we could clearly see that the magnetic structure was a striped order with an antiferromagnetic moment along the *c*-axis and that the wavefunction of a t_{2g} hole is strongly spin-orbit entangled, the J_{eff} =1/2 state (Fig. 1). The observed spin arrangement including the weak ferromagnetic moments along the *b*-axis is totally consistent with the theoretical work predicting isotropic-antiferromagnetic and anisotropic-ferromagnetic superexchange interactions across the corner- and edge-sharing bonds, respectively. Our results stimulate further exploration of a novel quantum spin state in iridates.

References

[1] D. Pesin and L. Balents, Nat. Phys. **6**, 376 (2010).
[2] B. J. Kim, H. Ohsumi, T. Komesu, S. Sakai, T. Morita, H. Takagi, and T. Arima, Science **323**, 1329 (2009).
[3] G. Jackeli and G. Khaliullin, Phys. Rev. Lett. **102**, 017205 (2009).
[4] K. Ohgushi, J. Yamaura, H. Ohsumi, K. Sugimoto, S. Takeshita, A. Tokuda, H. Takagi, M. Takata, and T. Arima, Phys. Rev. Lett. **110**, 217212 (2013).

Authors

K. Ohgushi, J. Yamaura, H. Ohsumi[a], K. Sugimoto[b], S. Takeshita[a], A. Tokuda[c], H. Takagi[d], M. Takata[a,b], and T. Arima[a,e]
[a]RIKEN SPring-8 Center
[b]Japan Synchrotron Radiation Research Institute, SPring-8
[c]Kwansei Gakuin University
[d]Department of Physics, University of Tokyo
[e]Department of Advanced Materials Science, University of Tokyo

Magnetism of Fe-Based Ladder Compounds

Ohgushi, Sato, Y. Ueda, and Uwatoko Groups

Since the discovery of superconductivity at high transition temperature in $LaFeAsO_{1-x}F_x$, the study of Fe-based superconductors has become a main stream in condensed matter physics. The basic structural feature of Fe-based superconductors is a square lattice of Fe atoms coordinated tetrahedrally by pnictogens or chalcogens. The most common magnetic structure realized in parent materials is a stripe order, which is stabilized by Fermi surface nesting and the orbital ordering. More recently, a block order was found in $A_2Fe_4Se_5$ (*A* = K, Rb, and Cs); an important feature of this ordered phase is a large magnetic moment 3.3 μ_B as a consequence of the strong electron correlation effect [1]. To gain further insights into the mechanism and variation of these magnetic orders, investigation of Fe-based compounds with various dimensions is important, because the dimensionality strongly influences the itinerancy of electrons.

We investigated electronic properties of Fe-based chalcogenides AFe_2Se_3 (*A* = Ba and Cs), in which Fe atoms form a quasi-one-dimensional ladder structure [2, 3]. Both compounds are Mott insulators due to prominence of the electron correlation effect in low-dimensional systems. The magnetic susceptibility shows anomaly corresponding to the magnetic order at 255 and 175 K for *A* = Ba and Cs, respectively. Interestingly, magnetic structures determined by neutron diffraction experiments are distinct in between:

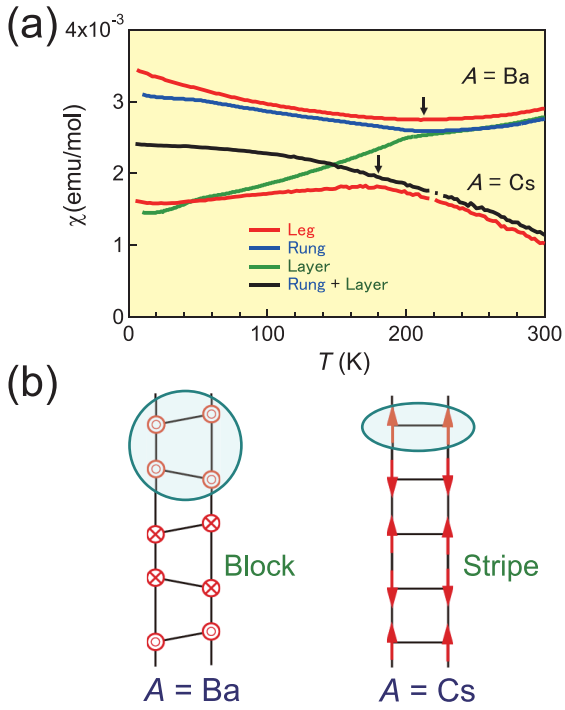

Fig. 1. (a) Temperature (T) dependence of the magnetic susceptibility (χ) at 5 T for Fe-based ladder compounds AFe$_2$Se$_3$ (A = Ba and Cs). (b) Magnetic structures determined by neutron diffraction experiments. Brock and stripe orders are realized in A = Ba and Cs, respectively.

whereas magnetic moments of 2.8 μ_B perpendicular to the ladder plane are arranged to form a Fe$_4$ ferromagnetic unit and each Fe4 stacks antiferromagnetically in A = Ba (block order), magnetic moments of 1.8 μ_B along the leg direction couple ferromagnetically and antiferromagnetically along the rung and leg directions, respectively, in A = Cs (stripe order). These magnetic properties are partly explained by recent Hartree-Fock calculations for the five-orbital Hubbard model [4]. Our results demonstrate that magnetism of Fe-based superconducting materials is rather complex owing to the multi-band effect and/or the electron correlation effect.

References

[1] P. Dai, J. Hu, and E. Dagotto, Nat. Phys. **8**, 709 (2012).
[2] Y. Nambu, K. Ohgushi, S. Suzuki, F. Du, M. Avdeev, Y. Uwatoko, K. Munakata, H. Fukazawa, S. Chi, Y. Ueda, and T. J. Sato, Phys. Rev. B **85**, 064413 (2012).
[3] F. Du, K. Ohgushi, Y. Nambu, T. Kawakami, M. Avdeev, Y. Hirata, Y. Watanabe, T. J. Sato, and Y. Ueda, Phys. Rev. B **85**, 214436 (2012).
[4] Q. Luo, A. Nicholson, J. Rincón, S. Liang, J. Riera, G. Alvarez, L. Wang, W. Ku, G.D. Samolyuk, A. Moreo, and E. Dagotto, Phys. Rev. B **87**, 024404 (2013).

Authors
K. Ohgushi, Y. Hirata, T. J. Sato, Y. Nambu, Y. Ueda, F. Du, S. Suzuki, Y. Uwatoko, K. Munakata, M. Avdeev[a], T. Kawakami[b], Y. Watanabe[b], H. Fukazawa[c], and S. Chi[d]
[a]Bragg Institute, Australian Nuclear Science and Technology Organization
[b]Nihon University
[c]Japan Atomic Energy Agency
[d]Oak Ridge National Laboratory

Mechanism of Enhanced Second-Harmonic Generation in Noncentrosymmetric Metal

Ohgushi, Suemoto, and Tajima Groups

Solids without spatial inversion symmetry attract great interests in the current condensed matter physics. The most common and well-studied systems without inversion symmetry are the ferroelectrics, where macroscopic polarization appears in an insulating state. Recently, conductive materials without inversion symmetry, which are known as noncentrosymmetric metals, have also attracted interest. In contrast to ferroelectrics, noncentrosymmetric metals do not exhibit macroscopic polarization due to screening by conducting electrons; instead the state is characterized by a higher-rank tensor (*e.g.* piezo-electric tensor). The breakdown of inversion symmetry is considered to influence the transport properties. For example, it is theoretically predicted that the inverse Faraday effect can be induced by Rashba interaction [1]. However, there have been few experimental studies [2], because noncentrosymmetric metals are rare.

We investigated electronic properties of a noncentrosymmetric metal $Pb_2Ir_2O_6O'$, which has the pyrochlore-type structure consisting of the Pb_2O' and Ir_2O_6 building units [3]. Structural analysis revealed that the structural distortion relevant to the breakdown of the inversion symmetry is dominated by the Pb_2O' unit but is very small in the Ir-O network. Nevertheless, gigantic second-harmonic generation (SHG) signal originating from the Ir 5d electrons, which is as large as SHG signals of GaAs, was observed. First-principles electronic structure calculations reveal that the

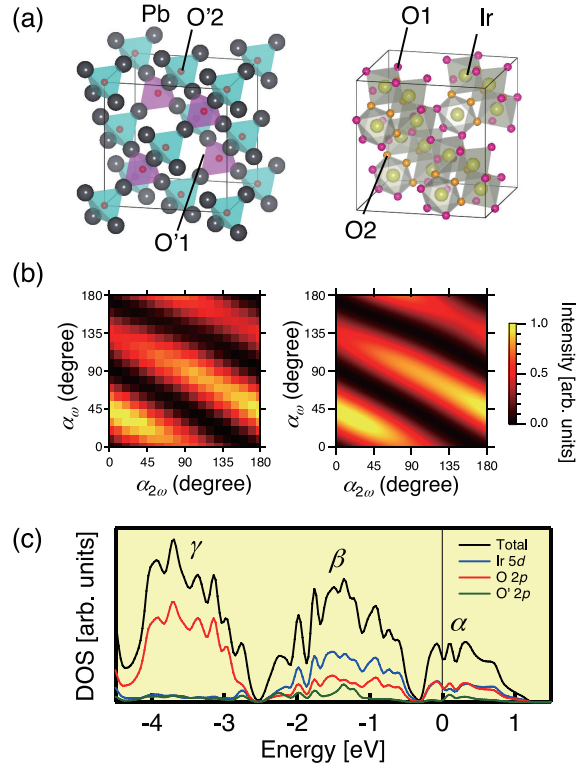

Fig. 1. (a) Crystal structure of $Pb_2Ir_2O_6O'$, which can be viewed as a sum of two interpenetrating units, Pb_2O' and Ir_2O_6. (b) Polarization dependence of the observed (left) and simulated (right) second-harmonic generation signals for $Pb_2Ir_2O_6O'$. α_ω and $\alpha_{2\omega}$ stand for polarization of incident and generated beams, respectively. (c) Total and partial density of states obtained from the first-principles calculation. SHG signals originate from dipolar transitions among the bands labeled as α, β, and γ. The large hybridization of O' 2p orbitals with α and β bands results in the observed large SHG signals.

underlying mechanism for this phenomenon is the induction of the noncentrosymmetricity in the Ir 5*d* bands by the strong hybridization with O' 2*p* orbitals, which are unique characteristics of Pb-containing pyrochlore-type oxides. Our results stimulate theoretical study of inversion broken iridates, where exotic quantum states such as a topological insulator and Dirac semimetal are anticipated.

References

[1] V. M. Edelstein, Phys. Rev. Lett. **80**, 5766 (1998).
[2] K. Ohgushi, J. Yamaura, M. Ichihara, Y. Kiuchi, T. Tayama, T. Sakakibara, H. Gotou, T. Yagi, and Y. Ueda, Phys. Rev. B **83**, 125103 (2011).
[3] Y. Hirata, M. Nakajima, Y. Nomura, H. Tajima, Y. Matsushita, K. Asoh, Y. Kiuchi, A.G. Eguiluz, R. Arita, T. Suemoto, and K. Ohgushi, Phys. Rev. Lett. **110**, 187402 (2013).

Authors

Y. Hirata, M. Nakajima[a], Y. Nomura[b], H. Tajima, Y. Matsushita[c], K. Asoh, Y. Kiuchi, A. G. Eguiluz[d], R. Arita[b], T. Suemoto, and K. Ohgushi
[a]Chiba University
[b]Department of Applied Physics, The University of Tokyo
[c]National Institute for Materials Science
[d]The University of Tennessee

---Division of Condensed Matter Theory----------

Superconductivity in a Correlated $E\otimes e$ Jahn-Teller System

Takada Group

The competition of electron-phonon (e-ph) and electron-electron (e-e) interactions in the mechanism of superconductivity is an old issue in strongly correlated systems and it has been investigated mostly in a single-orbital system, like the Hubbard-Holstein model in which the e-ph interaction enhances charge fluctuations, inducing an s-wave superconductivity in the vicinity of a charge density-wave (CDW) phase, whereas the e-e interaction suppresses such charge fluctuations but enhances spin ones, leading to a d-wave superconductivity near a spin density-wave (SDW) phase. If the effect of the e-ph interaction is about the same as that of the e-e interaction, there appears a rather complex nature of the pairing, namely, the off-site pairing (leading to either the extended s-wave or the d-wave nature, depending on the lattice structure) composed of not the bare electrons but the (phonon fully-dressed) polarons [1].

Here we add a further complication to this correlated and strongly phonon-coupled system by including the orbital degree of freedom. More specifically, we consider a two-dimensional (2D) square lattice with each site made of an $E\otimes e$ Jahn-Teller (JT) center, namely, a site composed of doubly degenerate orbitals like the e_g orbitals in the d bands which are coupled to the doubly-degenerate JT phonons. At each center, we also consider the e-e interaction in an appropriate way to make this JT crystal as a prototype of the charge-spin-orbital complexes. Then the Hamiltonian H of this system is given by $H=H_0+H_{\text{e-e}}+H_{\text{e-ph}}$, where H_0 is the noninteracting part composed of the electron hopping term characterized by the nearest-neighbor and next-nearest-neighbor hopping integrals, t and t', respectively, with keeping the orbital symmetry and the degenerate-phonon term with the phonon energy Ω_0. The orbital degree of freedom will be described by pseudospin for analogy to spin degree of freedom and the pseudospin symmetry is conserved throughout the crystal in this choice of H_0. Other terms, $H_{\text{e-e}}$ and $H_{\text{e-ph}}$, consist of local-site terms written with the intra-orbital Coulomb interaction U, the Hund's-rule coupling J, and the JT coupling g.

Due to the SU(2) symmetry in spin space and the conserved symmetry in pseudospin space, the Cooper pairing state can be specified by three quantum numbers; S the total spin of the pair, L the total pseudospin, and L_y its y component, making it possible to write the anomalous self-energy as $\Delta^S_{LLy}(k)$, where k is a combined notation of crystal momentum $\boldsymbol{k}$ and fermion Matsubara frequency $i\omega_n=i\pi T(2n+1)$ at temperature T with an integer n. Because of the rotational symmetry around the orbital-y axis, $L_y=\pm1$ states are degenerate and thus we treat only either $L_y=0$ or 1 here. The group theory determines the transformation property of $\Delta^S_{LLy}(k)$ in $\boldsymbol{k}$ space; it transforms in accordance with Γ, one of the irreducible representation of the point group C_{4v} (A_1, A_2, B_1, B_2, or E). The Pauli exclusion principle dictates that $\Delta^S_{LLy}(k)$ must be antisymmetric under two-electron interchange, indicating that Γ must be E for (S,L) equal to either (0, 0) or (1, 1); otherwise Γ must be either A_1, A_2, B_1, or B_2. With including this transformation property in Γ, we can easily write down the Eliashberg equation for $\Delta^S_{LLy}(k)$ at $T=T_c$ with the pairing interaction $V^S_{LLy}(q)$ containing the charge, spin, and orbital susceptibilities $\chi_c(q)$, $\chi_s(q)$ and $\chi_o(q)$, all of which are evaluated in the RPA with use of the irreducible susceptibility $\chi^o(q)$.

In Fig. 1, the phase diagram at $T=0.02t$ is plotted in the U-g plane for the typical case of $t'=0.125t$, $U=8t$, $J=t$, and $\Omega_0=0.10t$ at half filling. Two boundaries, denoted by L_{I} and L_{II}, indicates the lines where $\chi_o(q)$, and $\chi_s(q)$ diverge, respectively. In the close vicinity of these boundaries, those fluctuations are enhanced strongly enough to make the system enter into various superconducting phases, each labeled by $(\Gamma;S,L,L_y)$. Among them, we find (E;0,0,0) which is a novel chiral p-wave pairing state, $p_x(\boldsymbol{k})\pm ip_y(\boldsymbol{k})$, characterized by spin-singlet, orbital-singlet, and odd-parity in momentum space. This is a state very specific to the degenerate multi-orbital system and is induced by the cooperative effects of orbital and spin fluctuations that are, respectively, enhanced by e-ph and e-e interactions [2].

The conservation of the pseudospin symmetry is assumed in this study, but it is not always the case. By some tentative works, we come to know that the perturbation breaking this conservation will enhance T_c for the iron pnictides, while it reduces T_c very much for the vanadium oxides. This is an issue to be studied further in the future.

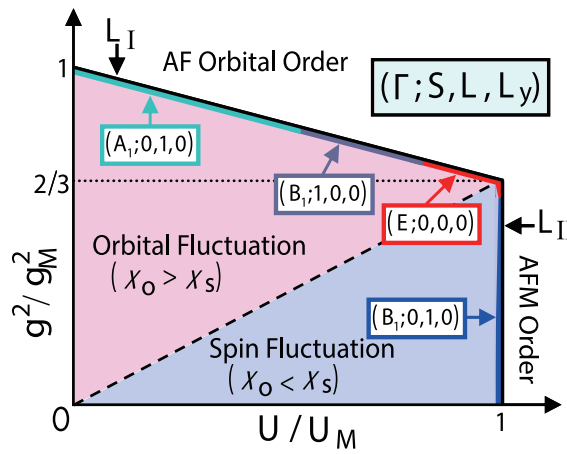

Fig. 1. Phase diagram in the U-g plane at half filling for $U/8=J=t$, $t'=0.125t$, and $\Omega_0=0.10t$ at $T=0.02t$. Units of strengths are so defined as $U_{\text{M}}=32/9\chi^0(\boldsymbol{Q},0)$ and $g_{\text{M}}^2/\Omega_0=1/\chi^0(\boldsymbol{Q},0)$, where $\boldsymbol{Q}$ [=(π,π)] is the momentum maximizing both $\chi_o(\boldsymbol{q},0)$ and $\chi_s(\boldsymbol{q},0)$.

References
[1] Y. Takada, J. Phys. Soc. Jpn. **65**, 1544 (1996).
[2] C. Hori, H. Maebashi, and Y. Takada, J. Supercond. Nov. Magn. **25**, 1369 (2012).

Authors
C. Hori, H. Maebashi, and Y. Takada

Dimensional Crossover in Layered *f*-Electron Superlattices

Oshikawa Group

Dimensionality plays a crucial role in condensed matter physics, especially in systems with strong interactions. Layered structures provide an opportunity to control the dimensionality and to observe effects of reduced dimensionality and crossover behavior between two and three dimensions. In particular, recent successful fabrications of the layered superlattices of $CeIn_3/LaIn_3$ [1] and $CeCoIn_5/YbCoIn_5$ [2] have opened new possibilities for investigating such phenomena in *f*-electron systems. In these systems, the *f*-electrons are present only in the Ce layers, which are 2-dimensional. These systems exhibit antiferromagnetic or superconducting long-range order in regions of the phase diagram, which implies a dimensional crossover to 3 dimensions. These observations also give rise to an even more fundamental question on the dimensionality of the heavy electron states, before formation of any order. Existing theories on these systems have been based on the assumption that the *f*-electrons, separated by the spacer layers, are almost decoupled, which results in essentially 2-dimensional heavy electron states.

We reexamined [3] the heavy electron states in the layered f-electron superlattices, based on the inhomogeneous dynamical mean field theory combined with numerical renormalization group as an impurity solver. We show that the spectral function exhibits formation of heavy electrons in the entire system below a temperature scale T_0. On the other hand, in terms of transport, two different coherence temperatures T_x and T_z are identified in the in-plane- and the out-of-plane-resistivity, respectively. Remarkably, we find $T_z < T_x \sim T_0$ due to scatterings between different reduced Brillouin zones. The existence of these two distinct energy scales implies a crossover in the dimensionality of the heavy electrons between two and three dimensions as temperature or layer geometry is tuned. This dimensional crossover would be responsible for the characteristic behaviors in the magnetic and superconducting properties observed in the experiments.

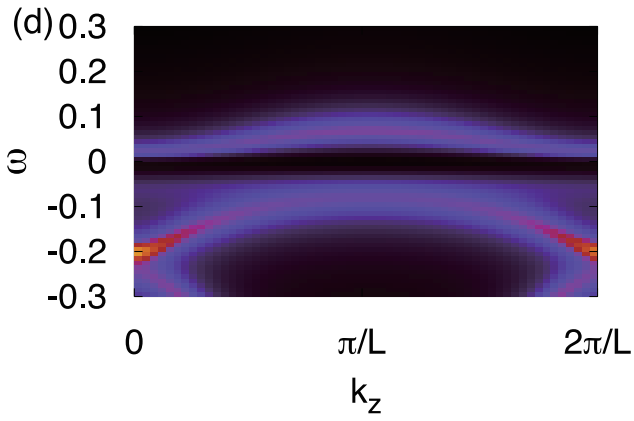

Fig. 1. Electron spectral function in a layered *f*-electron superlattice as a function of the momentum component k_z perpendicular to the layers, at a low temperature with fixed in-plane components k_x, k_y. The dispersion along the *z*-axis implies formation of heavy electron states extending over the entire system, coupled through the spacer layers which do not have *f*-electrons.

References
[1] H. Shishido, T. Shibauchi, K. Yasu, T. Kato, H. Kontani, T. Terashima, and Y. Matsuda, Science **327**, 980 (2010).
[2] Y. Mizukami, *et al.*, Nat. Phys. **7**, 849 (2012); S. K. Goh, *et al.*, Phys. Rev. Lett. **109**, 157006 (2012).
[3] Y. Tada, R. Peters, and M. Oshikawa, preprint (2013).

Authors
Y. Tada, R. Peters[a], and M. Oshikawa
[a]Kyoto University

Superconductivity near a Transverse Saturation Field in URhGe

Tsunetsugu Group

Ferromagnetic superconductivity in uranium-based heavy-fermion compounds has attracted much attention in condensed matter physics in the last decade. UGe_2, URhGe, UIr, and UCoGe show unconventional superconductivity within their ferromagnetic phases. Nonunitary superconductivity is believed to appear in these compounds and their pairing mechanism and symmetry as well as novel self-induced vortex states are central issues to be clarified in the modern theory of unconventional superconductors. Among these ferromagnetic superconductors, two isomorphic compounds, U*T*Ge (*T* = Rh, Co), exhibit superconductivity at ambient pressure within their ferromagnetic state and have a similar Ising-type anisotropy of magnetization. Spontaneous moment appears parallel to the *c* axis, and its magnetization curve exhibits meta-magnetic behavior with a notable mass enhancement when magnetic field **H** is applied to the *b* direction. This meta-magnetism is particularly prominent in URhGe and the moment gradually tilts with field and finally aligns parallel to **H** at h_s = 12 T. Superconductivity appears below the transition temperature T_{sc} = 0.24 K for **H** = **0**, and T_{sc} decreases with **H** and disappears at 2 T for **H** // b. Interestingly, superconductivity reappears above 8 T and shows the highest T_{sc} = 0.42 K at 12 T. The mechanism of this novel re-entrant superconductivity has not been fully clarified until now.

In this project, we propose a mechanism of the re-entrant superconductivity and analyze magnetic-field dependence of the spin-components of the superconducting order parameter. We point out that there are soft magnetic excitations near the transverse-saturation field h_s in these anisotropic systems as similar to the case in the transverse Ising system, and clarify how these soft excitations couple with itinerant electrons. We develop a weak-coupling theory of p-wave superconductivity in the presence of both ferromagnetism and magnetic field.

Figure 1 shows our result of temperature-magnetic field (h_x) phase diagram. Here, h_x represents the magnetic field strength in *b* direction. The superconducting transition temperatures for the polar state (T^x_{sc}) and that for the ABM state (T^{yz}_{sc}) are depicted. The amplitude of the gap Δ in the magnetic excitations and the tilting angle θ are also plotted in Fig. 1. In the low-field region, T_{sc} is suppressed as h_x increases and disappears due to orbital pair-breaking effects. In the high-field region near the saturation field h_s,

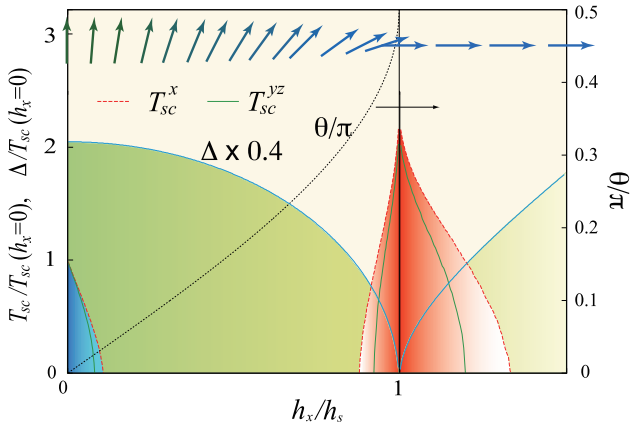

Fig. 1. Temperature - magnetic field (h_x) phase diagram. P-wave superconducting transition temperature for the polar state (T^x_{sc}) and that for the ABM state (T^{yz}_{sc}) are shown. The amplitude of the gap Δ in the magnetic excitations and the tilting angle θ of the ferromagnetic moments measured from the zero-field direction are also plotted. The transition temperatures are scaled by the value at h_x = 0, where T^x_{sc} = T^{yz}_{sc}. Arrows depict the change in direction of the ferromagnetic moment with magnetic field.

another superconducting phase appears and the transition temperature reaches a maximum at the saturation field and then is suppressed. As we commented above, the magnetic-excitation gap Δ gradually decreases with approaching h_s and vanishes at h_s. At the saturation field, the energy dispersion of the magnetic excitations is linear in the momentum, which represents the system is at a critical point. Above h_s, the excitations acquire a finite gap again and the gap increases linearly in h_x at higher fields.

The strong enhancement in the transition temperature near the saturation field arises from quantum critical fluctuations there and the nature of the fluctuations strongly restricts symmetry of the Cooper pairs. Analyzing the fluctuations near the saturation field, we find that the exchanging magnetic fluctuations between two electrons (Cooper pair) leads to electron spin flipping. Combining the fact that the Zeeman effects favor the equal-spin pairs and now the spin is not conserved in the presence of the transverse field, the dominant superconducting order parameter is a linear combination of the two equal-spin pairing states. This state is completely different from that in the low field superconducting state, where only one of the equal-spin pairing states is realized due to the strong Zeeman effects by the ferromagnetism.

The phase diagram we have determined is qualitatively consistent with that in URhGe. Experimental determination of the superconducting order parameters near the saturation field is an interesting subject in the future progress for understanding the ferromagnetic superconductivity in URhGe. For more quantitative analyses, it is important to include longitudinal spin fluctuations, which have been observed in UCoGe. Such longitudinal fluctuations would play an important role for realizing meta-magnetic behaviors near the saturation field in URhGe.

Reference

[1] K. Hattori and H. Tsunetsugu, Phys. Rev. B **87**, 064501 (2013).

Authors
K. Hattori and H. Tsunetsugu

Development of Novel First-Principles Methods for Material Research

Sugino Group

The first-principles computational methods have enabled, with increasing precision, to elucidate properties of matters starting from the microscopic quantum principles only. This was strongly driven by the development of supercomputers and the computational theory, *e.g.*, density functional theory (DFT) and Hartree-Fock. Those theories have already matured and great many efforts are now made toward the development of post-DFT theory and the extension of the frontier of DFT applications. Towards the goal, our group has made three important steps. The first one is the development of a post-DFT scheme, which is based on the tensor compression technology to compactly represent the many-body wave function. A graduate course student, Wataru Uemura, showed that the canonical decomposition algorithm indeed greatly facilitates handling of the wave function that appears in the full configuration interaction (CI) scheme. The developed scheme [1], called symmetric tensor decomposition (STD), is considered make the full CI a method of choice for the molecular and some of the condensed matter researches.

The use of the tensor compression technology itself is not new, but was established as a powerful method to handle one-dimensional spin and Hubbard systems some years ago. The STD-CI, however, applied the technology to the conventional molecular orbital theory and, with algorithmic improvements, has greatly reduced the memory and the computational time requirement. It is also anticipated that, by combining STD-CI with the tensor network theory developed in the spin physics, extended systems will become the target of study. Despite the improved efficiency, the computational time is yet prohibitively large even for medium-sized molecules, but is expected to become tractable by the next-generation supercomputers because of its excellent parallelizability.

Towards the study of electronically excited states, the research associate, Yoshifumi Noguchi parallelized the code for many-body perturbation theory, or a post-DFT theory, for the K-computer and the ISSP supercomputer. The excited-states of a molecule containing up 100 atoms, such as fullerenes, has become the target of study [2]. By combining with the DFT-based schemes [3], we are advancing the method for excited-state research.

Our group regards the solid-liquid interface is the important application field of DFT. We are particularly interested

$$\Psi(x_1, x_2, \cdots, x_N) = \sum_{I=1}^{{}_M C_N} A_I^0 \Phi_I^0(x_1, x_2, \cdots, x_N)$$

Non-interacting

$$\sum_{I=1}^{K} A_I^{STD} \Phi_I^{STD}(x_1, x_2, \cdots, x_N)$$

Interacting

Fig.1: An electronic wave function has been traditionally expanded by non-interacting terms (Φ^0) in the configuration interaction (above). The series can be greatly shortened when expanded by interacting ones (below). The tensor decomposition provides a practical way to construct a maximally compact series, allowing thereby accurate numerical handling of the wave function. Using this novel algorithm, or STD-CI, we are developing a code for electronic structure calculation to be used in the next-generation supercomputer.

in explaining the energy conversion mechanism as typified by the fuel-cell reactions. The major object of the fuel-cell science is to relate the bias potential with the electrocatalytic reactions, which has been hampered by the difficulty of applying the bias potential to the interface. Important algorithmic improvements were made by the collaboration with research group in AIST to keep applying the bias potential throughout the DFT-based molecular dynamic simulation [4]. Those methods are now used for the large-scale simulations on K-computer.

References

[1] W. Uemura and O. Sugino, Phys. Rev. Lett. **109**, 253001 (2012).
[2] Y. Noguchi, O. Sugino *et al*., J. Chem. Phys. **137**, 24306 (2012).
[3] T. Tsukagosi *et al*., Phys. Rev. B **87**, 35421 (2012); Phys. Rev. A **86**, 64501 (2012).
[4] N. Bonnet *et al*., Phys. Rev. Lett. **109**, 266101 (2012).

Authors

O. Sugino, Y. Noguchi, N. Bonnet, T. Tsukagoshi, and W. Uemura

Relaxor Behavior and Morphotropic Phase Boundary in a Simple Model

Kato Group

Ferroelectric relaxors made from perovskite oxides (ABO_3) have attracted much interest because of their characteristic dielectric properties suitable for application. The common feature of perovskite-type relaxors is intrinsic randomness due to compositional disorder. It is well known that structural phase transition induced by change in composition plays a special role for obtaining excellent dielectric properties; the region near this phase transiton is called the morphotropic phase boundary (MPB).

The origin of large dielectric response at the MPB was discussed within the Landau-Ginzburg-Devonshire (LGD) theory. The LGD theory is, however, not satisfactory to describe the whole properties of relaxors since it treats only spatially-averaged quantities. In particular, important information on spatial profiles of electric polarization such as domain structure and spatial inhomogeneity due to compositional disorder cannot be discussed by the LGD theory.

In order to understand physics near the MPB, we have performed large-scale Monte Carlo simulation [1] to a simplified dipole model on a square lattice given as

$$\mathcal{H} = \sum_{i<j} \left[\frac{\boldsymbol{\mu}_i \cdot \boldsymbol{\mu}_j}{r_{ij}^3} - 3\frac{(\boldsymbol{\mu}_i \cdot \boldsymbol{r}_{ij})(\boldsymbol{\mu}_i \cdot \boldsymbol{r}_{ij})}{r_{ij}^5} \right].$$

Here, $\boldsymbol{\mu}_i$ is a three-dimensional vector representing an electric polarization caused by the ionic displacement at site i, and $\boldsymbol{r}_{ij}$ is a displacement vector from site i to j. In order to represent intrinsic compositional randomness at B-site in perovskite oxides, we divide the square lattice into two sub-lattices, A and B as shown in the inset of Fig. 1(a), and assume that magnitude of the A-site dipole moments is fixed as unity (μ_A =1), whereas that of the B-site dipole moments has spatial distribution. The magnitude of the B-site moment is chosen randomly as μ_B = max(0.8-0.1n,0), where n is an integer-valued random variable following the Poisson distribution $P(n) = \lambda^n \exp(-\lambda)/n!$. We have performed Monte Carlo calculation by using efficient O(N) algorithm optimized for long-rage interaction [2].

In Fig. 1(a), we show real part of calculated dielectric susceptibilities as a function of the temperature T. The

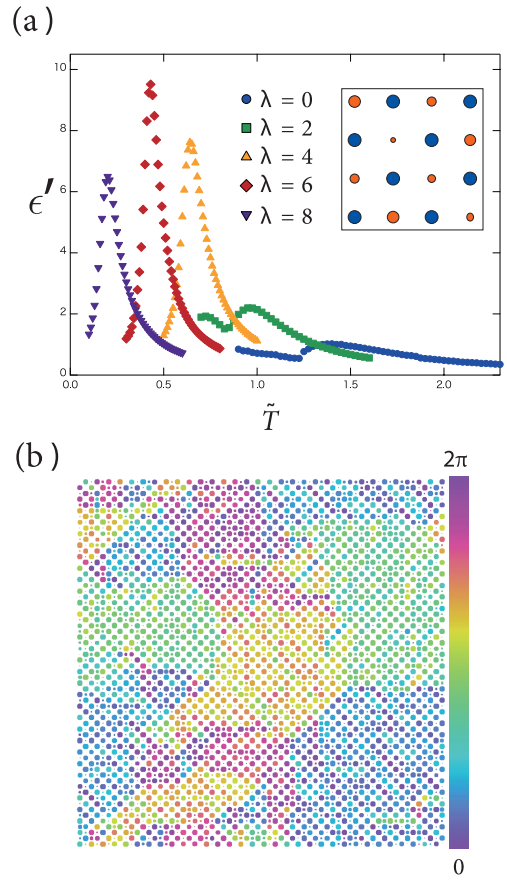

Fig. 1. (a) Plot of real part of dielectric susceptibilities per site. Data are horizontally shifted for each value of λ. (Inset) Blue and red circles indicate A- and B-sublattice on a square lattice. (b) A snapshot of dipole configurations for λ=6. Sizes of radii represent sizes of projected dipole moments, and colors of circles indicate directions of dipole moments.

peak of the dielectric susceptibility is well suppressed for small λ, whereas it rapidly grows with increasing λ. The maximum value becomes largest at an optimum value λ=5-6, and is reduced for larger value of λ. These features well resemble the behavior of the dielectric response near MPB in perovskite oxides, identifying λ=5-6 to be the MPB.

To examine mechanism of emerging of the maximum, a snapshot at λ=6 is shown in Fig. 1(b). We observe meso-scale ferroelectric domain, whose size becomes significantly large near λ=5-6. This remarkable enhancement of correlation length for ferroelectric ordering, indicated from the snapshot, is due to phase competition. For small λ, anti-ferroelectric phase is stabilized at low temperatures, whereas relaxor ferroelectric phase is realized for large λ. Direction of polarization is diagonal in the former phase, and is along neighboring sites in the latter phase. As a result, the easy-axis potential is mixture of the ones of these two phases near the MPB (λ=5-6). The resulting mixed potential forms the dimple at the bottom of a wine bottle, and it makes dipoles easy to rotate. This result indicates that *local* polarization rotation under suppressed anisotropy makes domain wall *flexible* to external field, leading to huge dielectric response.

In summary, we proposed a simple dipole model, and executed Monte Carlo simulations to it. We showed that there appears a boundary ferroelectric phase between two phases, and that it has large ferroelectric domains with flexible walls. Our result near the MPB can be related to recent experiments by neutron scattering [3] and transmission electron microscopy [4].

References
[1] Y. Tomita and T. Kato, J. Phys. Soc. Jpn. **82**, 063002 (2013).
[2] K. Fukui and S. Todo, J. Comp. Phys. **228**, 2629 (2009).
[3] M. Matsuura, K. Hirota, P. M. Gehring, Z.-G. Ye, W. Chen, and G. Shirane, Phys. Rev. B **74**, 144107 (2006).
[4] K. Kurushima and S. Mori, Materials Science and Engineering **18**, 092015 (2011).

Authors
Y. Tomita[a] and T. Kato
[a]Shibaura Institute of Technology

---Division of Nanoscale Science----------

Corbino Thermopower of Quantum Hall Systems

Iye Group

Thermopower is known to be a sensitive probe to investigate properties of electron systems, owing to its direct access to the energy derivative of the density of states (DOS) and to the entropy of the systems. It has been predicted [1, 2] that the radial thermopower S_{rr} measured in the Corbino geometry (Fig. 1b) exhibits behaviors qualitatively different from the longitudinal thermopower S_{xx} measured in the Hall-bar geometry in the quantum Hall (QH) systems. Notably, in the QH plateau regions where the longitudinal conductivity $\sigma_{xx}=\sigma_{rr}$ vanishes, S_{xx} also vanishes, whereas S_{rr} is expected to take large values changing sign at the center of the QH plateau. The measurement of S_{rr} thus provides us with a unique opportunity to probe the entropy of the system in the QH plateau regions [2]. The measurement of thermopower in the QH systems, however, has predominantly been performed on the Hall-bar geometry. In the present study, we make measurements of the diffusion thermopower S_{rr} in the Corbino geometry [3].

Thermopower generally contains contributions from two distinct mechanisms: diffusion and phonon drag. In the QH systems embedded in GaAs/AlGaAs wafers, it is well known that the latter contribution outweighs the former by orders of magnitude, if the temperature gradient is introduced by an external heater. The high sensitivity to the DOS and entropy, however, is expected only for the former. In order to measure the diffusion contribution selectively, we employ microwave-heating technique [4] (Fig. 1a) in the present study; microwaves injected into the coplanar wave guide (CPW) placed on the surface of the wafer capacitively couple with the two-dimensional electron gas (2DEG) beneath the slots of the CPW and locally heats the electrons. The lattice temperature remains intact, eliminating the phonon-drag contribution. As depicted in Fig. 1b, we install CPW along the outer periphery of a Corbino disk, which introduces radial temperature gradient toward the center electrode, leading to the radial thermopower S_{rr}.

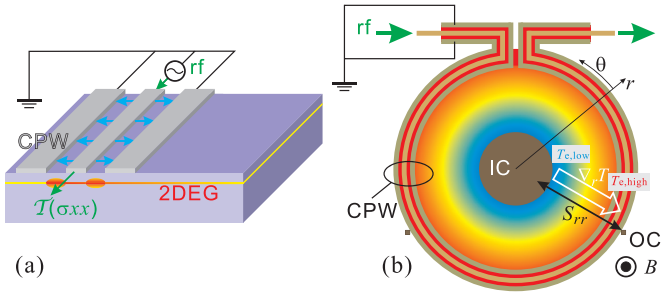

Fig. 1. Schematic diagrams of (a) coplanar wave guide (CPW) used in the microwave-heating technique and (b) Corbino device to measure diffusion thermopower S_{rr}. IC: inner contact. OC: outer contact. The microwaves (rf) propagating through the CPW placed on the surface are partially absorbed by the two-dimensional electron gas (2DEG) underlying the slot of the CPW and heats the electrons. In the Corbino device, electrons near the outer periphery of the disk are heated by the CPW, generating the concentric temperature gradient toward IC.

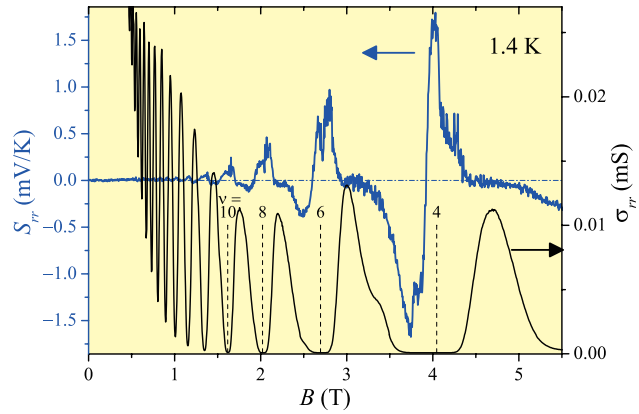

Fig. 2. Thermopower S_{rr} (left axis) and the conductivity σ_{rr} (right axis) measured in the Corbino device. Vertical dashed lines indicate the positions of the center of the QH plateau (exact even integer fillings ν).

The measured S_{rr} is plotted in Fig. 2 along with σ_{rr} obtained in the same Corbino device. As can be seen in the figure, S_{rr} takes large values (~ ±1 meV/K) in the regions where σ_{rr} = 0, alternating the sign at exact even integer fillings marked by vertical dashed lines, in accordance with the theoretical prediction mentioned above. Noting that S_{rr} represents entropy per carrier [2], large values of $|S_{rr}|$ can be understood as reflecting the fact that only small numbers of thermally activated carriers are available in the QH plateau regions. The positive (negative) sign of S_{rr} indicates that the carriers are hole-like (electron-like) for the fillings ν just below (above) integer values.

References
[1] H. van Zalinge, R. W. van der Heijden, and J. H. Wolter, Phys. Rev. B **67**, 165311 (2003).
[2] Y. Barlas and K. Yang, Phys. Rev. B **85**, 195107 (2012).
[3] S. Kobayakawa, A. Endo, and Y. Iye, J. Phys. Soc. Jpn. **82**, 053702 (2013).
[4] A. Endo, T. Kajioka, and Y. Iye, J. Phys. Soc. Jpn. **82**, 054710 (2013).

Authors
S. Kobayakawa, A. Endo, and Y. Iye

Switching of Andreev Current with Spin-Hall Effect

Katsumoto Group

Two-dimensional electron gas (2DEG) in InAs quantum well has been often adopted as a material for middle layers in Superconductor-Normal conductor-Superconductor (SNS) sandwiches due to its low Schottky barrier to metals. At the same time it is well-known that the spin-orbit interaction (SOI) is generally strong in such materialswith narrow band gaps and InAs 2DEG actually shows spin-interference phenomena due to strongRashba-type SOI. The spin Hall effect originates from the SOI draws apart a spin up-down pair of electrons to form a Cooper pair, thus is supposed to work against the Andreev reflection, and to affect the SNS transport or the Andreev bound states (ABSs) formed in the normal layer.

Here we report suppression of electric current enhanced by Andreev reflection with transverse current flow, which breaks the time-reversal symmetry in two-dimensional system (2DES) of InAs. The inset of Fig.1 schematically shows the sample structure, in which a 200nm wide InAs 2DES stripe is sandwitched by two Nb electrodes. The sample was cooled down to 0.5K. During the electric measurement, we kept the crossing point of Nb and InAs 2DES at the ground level. In order for that, we formed circuits for sweeping the potentials of the four terminals assuming Ohmic contact resistances.

At zero magnetic field and with no transverse current, the differential conductance oscillates with the source-drain voltage V_{sd} making a large peak structure at the origin. The characteristic lineshape can be interpreted with assuming the formation of ABSs as follows. The zero-bias peak reflects the resonance between the two Fermi levels of superconducting electrodes via the virtual tunneling through ABSs while the two side peaks are direct resonances between one of the superconductors and an ABS. Because the mean free path of InAs 2DES exceeds the width of the 2DES strip, the transport between the two Nb electrodes should be ballistic, that is, ABSs should be formed.

In Fig.1(a) we show the response to the magnetic field, in which the structure is squeezed to the origin and disappears at 0.75T. This behavior manifests that the structure is superconductivity origin and we can explain it with considering some kind of interference effect. Because the additional phase due to the voltage accumulates for Andreev type (electron-hole) shuttling, the Aharonov-Bohm (AB) phase should shift the positions of ABSs. Figure 1(b) shows the differential conductance (G) again as a function of V_{sd} with the transverse currents through the InAs 2DES strip from 108 nA to 1.2 μA. The transverse current also strongly diminishes the G-V_{sd} structure. The difference between the response to the magnetic field and that to the transverse current is apparent. This suggests that the latter comes not from the orbital effect and that the spin-Hall effect induced by the transverse current reduces the formation of ABSs.

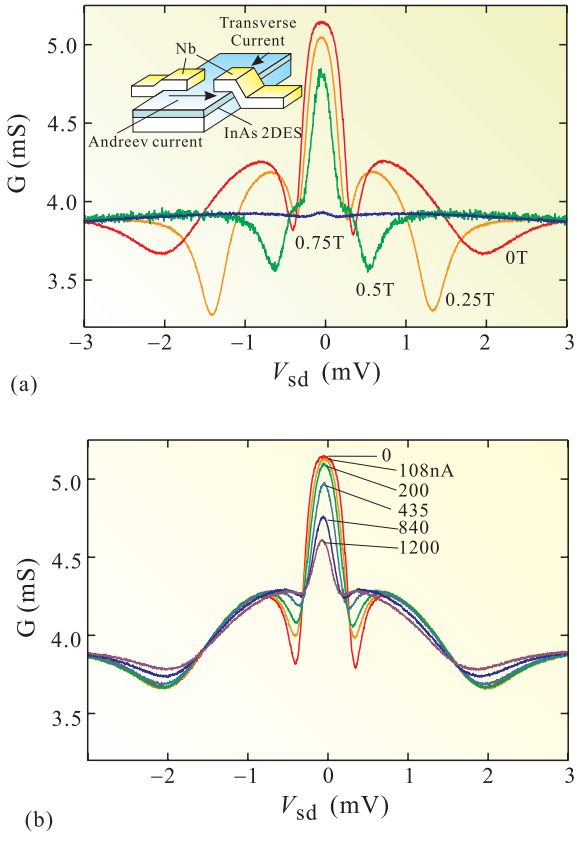

Fig. 1. (a) Differential conductance of Nb-InAs-Nb SNS junction at 0.5K as a function of the source-drain bias voltage. The parameter is the external magnetic field perpendicular to the sample. The inset shows schematic view of the sample. (b) The same measurements as those in (a) under zero magnetic field with transverse currents through the InAs strip from zero to 1.2μA.

Reference

[1] Y. Takahashi, Y. Hashimoto, Y. Iye, and S. Katsumoto, J. Cryst. Growth, published online: http://www.sciencedirect.com/science/article/pii/S0022024813000705.

Authors

S. Katsumoto, T. Nakamura, and Y. Hashimoto

A Novel Method to Verify Spin Diffusion Length

Otani and Kato Groups

Spin relaxation and spin dephasing are the central issues in fields of quantum information and spintronics as they determine how far an electron can transfer spin information, i.e., the spin diffusion length. The spin diffusion length is thus an essential parameter in terms of application in future spintronics devices. However, there is no well-established method for obtaining this length; values reported so far differ greatly depending on the experimental method employed, the number of variables involved in the definition of the spin diffusion length and so on. Since the spin diffusion length determines the spin Hall angle, which is one of the most important physical quantities in spintronics, it is of great importance to evaluate this length correctly.

In a conventional method, a lateral spin valve structure where a weak spin-orbit (SO) material such as Cu is bridged by two ferromagnets is used to determine the spin diffusion length. On the other hand, this conventional method cannot be applied to a strong SO material such as Pt, since the spin diffusion length is in general of the order of nanometers. One of the ways to obtain such a short spin diffusion length is to use the spin absorption technique as shown in Fig. 1(a) [1]. However, there was a big debate about how to evaluate the spin diffusion length of a strong SO material [2] because there are several parameters that determine the spin diffusion length, which hinders straightforward evaluation.

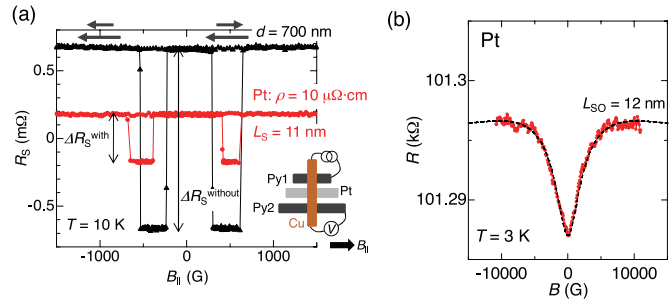

Fig. 1. (a) Nonlocal spin valve (NLSV) signal with a 20 nm thick Pt wire (ΔR_S^{with}) in between two Permalloy (Py) wires. As a reference signal, we also plot the NLSV signal without the Pt wire ($\Delta R_S^{without}$). The magnetic field is applied parallel to the Py wires. From the ratio of $\Delta R_S^{with}/\Delta R_S^{without}$, the spin diffusion length of Pt can be evaluated (L_S = 11±2 nm). A pair of arrows on the top indicates the magnetizations of Py1 and Py2. The inset shows the schematic of our lateral spin valve device. (b) WAL curve of a 20 nm thick Pt wire measured at T = 3 K. In this case, the magnetic field is applied perpendicular to the plane. The broken line is the best fit of Hikami-Larkin-Nagaoka formula. From the fitting, the SO length of Pt can be obtained (L_{SO} = 12±3 nm).

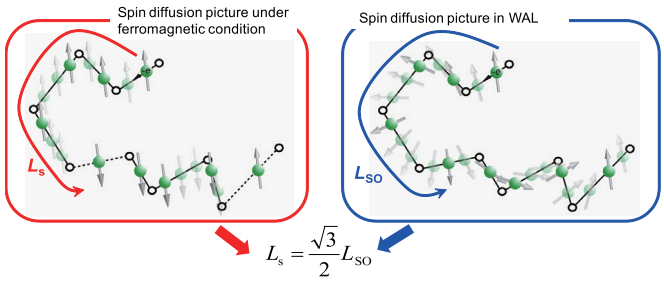

Fig. 2. Spin diffusion lengths measured with ferromagnets (L_S; left) and obtained from WAL measurement (L_{SO}; right). The relation of the two length scales ($L_S = \sqrt{3}/2\, L_{SO}$) has been experimentally verified.

Otani group in collaboration with Kato group have discovered a new way to evaluate the spin diffusion length [1]. In the new method, the spin diffusion length can be evaluated just by measuring very precisely the resistance of a SO material (see Fig. 1(b)). In metals, electrons are weakly localized at temperatures approaching absolute zero. When there is a finite SO interaction, the weak localization changes into weak antilocalization (WAL) and the magnetoresistance strongly depends on the SO interaction. In the present work, we focused on this dependency and obtained the spin diffusion lengths of several materials such as Cu, Ag and Pt. The values obtained with the new method are quantitatively consistent with those from the conventional methods. Since the new method reduces the number of variables involved in determining spin diffusion length, a more accurate value can be calculated. In addition, it has been shown theoretically that the spin diffusion length in a localized state and under ferromagnetic conditions varies slightly (by a factor of $\sqrt{3}/2$). We have experimentally verified for the first time the relationship between the spin diffusion length in a localized state and under ferromagnetic conditions (see Fig. 2). Thanks to these results, a vigorous debate on the spin diffusion length can be concluded and this new method will play an important role in the fields of quantum information and spintronics.

Reference
[1] Y. Niimi, D. H. Wei, H. Idzuchi, T. Wakamura, T. Kato, and Y. Otani, Phys. Rev. Lett. **110**, 016805 (2013).
[2] L. Liu, R. A. Buhrman, and D. C. Ralph, arXiv:1111.3702.

Authors
Y. Niimi, D. H. Wei, H. Idzuchi, T. Wakamura, T. Kato, and Y. Otani

Bias-Dependent Atomic STM Images and Electronic Structure at Au-Adsorbed Ge(111) Surface

Komori Group

The Au-adsorbed Ge(111) surface has two surface metallic bands with hexagonal Fermi surfaces [1]. One band is electron-like and the other is hole-like. The former band is anisotropically split and spin-polarized owing to strong spin-orbit interaction at the surface. These features have been studied by angle-resolved photoemission spectroscopy (ARPES). Figure 1(a) shows the ARPES intensity map along $\Gamma_0 - M - \Gamma_1$ line for the surface with 0.9 ML of Au on average. The observed electronic states including the surface bands (S_1, S_2 and S_5) are qualitatively consistent with the bands calculated for an optimized conjugate honeycomb-

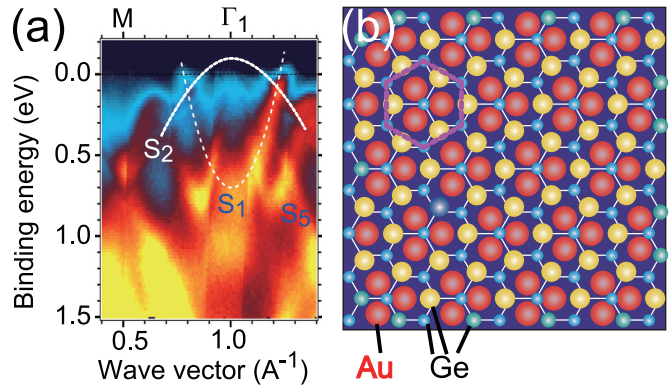

Fig. 1. (a) ARPES intensity map showing the band structure of the Au-adsorbed the Ge(111) surface. Three surface bands S_1, S_2 and S_5 are seen, and white dashed lines are guides to the eye for the S_1 and S_2 bands. (b) Schematic top-view CHTC model for the Au-adsorbed Ge(111) surface. The white hexagonal lattice indicates the subsurface bilayer Ge lattice, the small blue balls the lower Ge atoms of the bilayer, small green the upper Ge atoms of the bilayer, yellow the surface Ge atoms, and red the surface Au atoms. Three adjacent Au atoms make an Au trimer, which is imaged as a single protrusion in Fig. 2(a). Centers of three adjacent Ge atoms are imaged as protrusions in Fig. 2(b), and make a honeycomb pattern, which is indicated as the magenta hexagon.

chained-trimer (CHCT) structure model shown in Fig. 1(b) [2]. However, there have been two discrepancies between the experiments and theories; the STM image at low bias voltage (V_{sb}) and the bottom energy of the S_1 band. In the present study, we clarify how these are solved by considering the surface electronic structure and the doping by triangular nanoclusters observed on the surface.

Figure 2 shows bias-dependent atomic STM images. The images were observed at 80 K for the surface with 1.2 ML of Au atoms on average. The STM image for V_{sb} = 2.0 V (Fig. 1(a)) shows a triangle lattice pattern with a triangular nanocluster. For V_{sb} = 0.1 V (Fig. 1(b)), a honeycomb pattern appeared on the same surface area, and the position of the triangular nanocluster was imaged as a dented area. The triangle lattice is consistent with the arrangement of the Au trimers on the surface in the CHCT model shown in Fig.

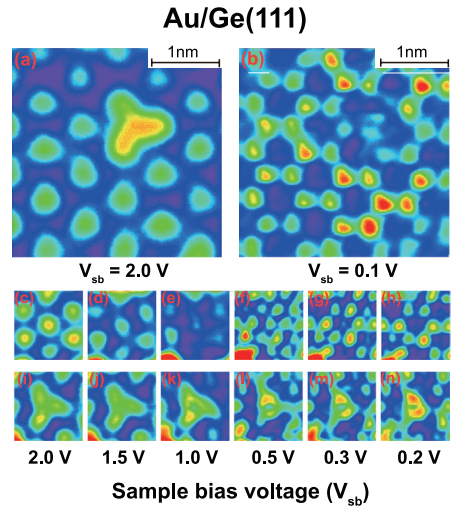

Fig. 2. STM images of the Au-adsorbed Ge(001) surface showing sample-bias-voltage (V_{sb}) dependence. Triangle lattice pattern in (a) is attributed to the arrangement of the surface Au trimers. (See Fig. 1(b)). In (b), atomic protrusions arrange in a honeycomb pattern. The same area is imaged in (a) and (b). A triangular nanocluster is seen as a protrusion in (a) while it is imaged as a dented area in (b). The precise bias dependence of the lattice pattern and the triangular nanocluster is shown in (c-h) and (i-n). Both the triangle and honeycomb patterns coexist for V_{sb} = 0.5 V as in (f). The triangular nanocluster becomes thin with decreasing V_{sb}.

1(b) whereas the honeycomb pattern could not be attributed to any arrangement of the surface Au and Ge atoms in the model. Bias-dependent STM images shown in Figs. 2(c-h), and 2(i-n) indicate gradual change of the lattice pattern and the triangular nanocluster, respectively.

It was theoretically shown that the surface Au trimers of the CHCT model make the electron-like (S_1) band. The hole-like (S_2) band, on the other hand, originates from the surface and subsurface Ge atoms. The energy maximum of the S_2 band is 0.1 eV above Fermi energy. Consequently, the local density of states around the surface Ge atoms can be high at the top energy of the S_2 band. This causes a honeycomb lattice pattern of the protrusions due to the surface Ge atoms in the STM images as observed for $V_{sb} < 0.3$ V. The bottom of the S_1 band decreases with increasing the surface density of the triangular nanocluster. It plays a role of the dopant selective to the S_1 band although its atomic structure is unknown [3].

References

[1] K. Nakatsuji *et. al*., Phys. Rev. B **80**, 081406 (2009).
[2] K. Nakatsuji *et. al*., Phys. Rev. B **84**, 035436 (2011).
[3] K. Nakatsuji *et. al*., J. Phys. Condens. Matter **25**, 045007 (2013).

Authors

K. Nakatsuji, Y. Motomura, R. Nikura, and F. Komori

Development of Versatile Nanoscale Potentiometry for Visualizing Distribution of Electrical Resistance

Hasegawa Group

Scanning tunneling microscopy (STM) has been utilized for imaging atomic structure of surfaces. Combined with a function of tunneling spectroscopy, the probe microscopy can also visualize spatial distribution of various properties in nanoscale; superconductivity has been detected and visualized through the observation of the superconducting gap. A spin-polarized probe tip picks up signals of local magnetization, and inelastic tunneling provides the energy of spin flipping and transition between spin states of atomic and nanosize systems. Here, we introduce another unique function of STM; mapping of electrical potential and resistance in nanometer-scale spatial resolution.

The method called scanning tunneling potentiometry enables us to observe spatial distribution of the the potential of a sample surface under current flow across the sample, as well as its topographic STM image. Under current flow, which is 1 ~ 2 mA in the present case, the potential or the Fermi level changes locally at the places where electrical resistance there. Figure 1 shows an example of the topographic and potential images taken simultaneously on a 2-mm-wide and 2-nm-think Au thin film. As shown in the topograph, Au grains whose size is 10 to 30 nm are randomly distributed. The potential image, however, clearly reveals steps in the potential, which provide direct evidence of significant resistance there. The sites of the drops exactly correspond to boundaries between the Au grains, as proved by a comparison of the two images. Not all domain boundaries, however, induce the potential drop, although the boundaries that induce the potential drops do not show any structural differences discernible in the STM image from those that do not induce the drops. We confirmed that the

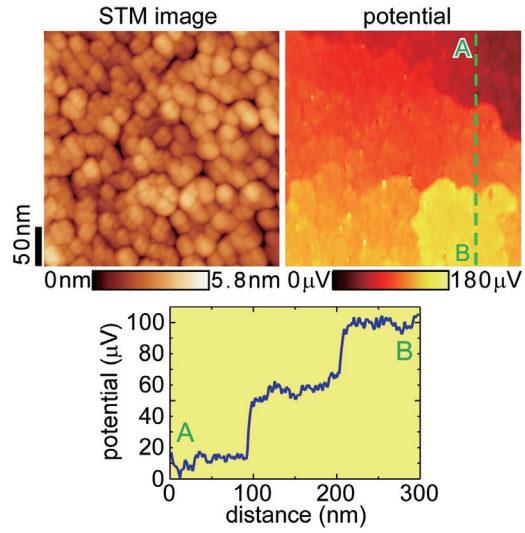

Fig. 1. STM image of a 2-nm-thick Au thin film and its potential mapping taken simultaneously under current flow (1~2 mA) from the bottom to the top of the images. A cross-sectional plot of the potential indicates that potential drops, which correspond to electrical resistance, occurs at grain boundaries and that the potential can be measured with a resolution of ~5 μV.

observed drops are really due to the electrical potential by taking the images under the reversed current flow across the sample; the direction of the potential drops is also reversed with the reversed current. The reversed potential image also indicates that the sites and magnitude of the potential drops do not change significantly in the both directions of the current flow.

The magnitude of the potential drops can be estimated as ~ 40 μV from the cross-sectional plot shown in Fig. 1(c). The plot also indicates that the noise level of the potential is ~ 5 μV even at room temperature. The resolution is quite high compared that of other STM-related potential measurement methods, such as Kelvin probe force microscopy, with which we detected interatomic charge transfer [1], and the method of measuring energy levels of electronic states that was used for visualizing the Friedel oscillation [2]. The reason of the high resolution is because of the zero-balance method used in the potential measurement; the potential is measured from the voltage applied on the sample to make the tunneling current zero.

One drawback is that the method can only be applied to metallic samples; in the case of semiconducting samples, the tunneling current is zero within the band gap and therefore the bias voltage that makes the tunneling current zero cannot be determined with high energy sensitivity. In this work, we have developed a new method with which one can take a potential mapping on semiconducting samples [3], which will obviously extend versatility of this technique.

We are applying the method to study potential profiles on surface conductive layers, which are the ultimate two-dimensional electron systems. Superconductivity even on one-monolayer-metal-induced reconstructed surfaces was reported. Our study will reveal roles of various structural defects on the (super-) conductance in real space. By using a spin-polarized tip, one can also detect spin current since the dispersionless current is caused by the potential difference between the two spin directions. We expect that various spin relaxation processes will be identified in real space and attributed to local structures using this method.

References
[1] T. Eguchi, *et al*., Phys. Rev. Lett. **93**, 266102 (2004).
[2] M. Ono, *et al*., Phys. Rev. Lett. **96**, 016801 (2006).
[3] M. Hamada and Y. Hasegawa, Jpn. J. Appl. Phys. **51**, 125202 (2012).

Authors
M. Hamada and Y. Hasegawa

Oxide Photocatalysts

Lippmaa Group

Perovskite-type titanates have been proposed as potentially efficient photocatalytic energy conversion materials that can absorb visible sunlight and directly transfer the formed photocarriers to liquid water, thereby generating hydrogen gas. Despite the potential for efficient, cheap, and sustainable energy conversion, photocatalytic materials have so far not reached practical solar light collection efficiencies. The main reason appears to be the high recombination rate of generated photocarriers, which means that the energy of the sunlight is mostly spent on generating heat, rather than splitting water. The purpose of this work was to determine the electronic structure of Rh-doped $SrTiO_3$, which is known to be a moderately efficient hydrogen-evolution photocatalyst.

For efficient transfer of photoelectrons from a bulk photocatalyst to water, it is necessary to have a semiconductor with a conduction band located well above the reduction potential of water, while the band gap should be close to 2 eV for the best energy harvesting efficiency. Pure $SrTiO_3$ is a wide-gap semiconductor that satisfies the conduction band alignment requirement with water, but it is transparent for visible light and only absorbs sunlight in the ultraviolet part of the spectrum, above the band gap energy of 3.2 eV. Rhodium doping of the $SrTiO_3$ host semiconductor appears to be quite special, in that it creates deep impurity levels either around the mid-gap region of $SrTiO_3$ or close to the top of the valence band without affecting the location of the conduction band edge. Electrochemical measurements under visible light show an apparent *p*-type photocathode behavior, which is quite unusual for typically *n*-type $SrTiO_3$. In this work, we have used a combination of x-ray photoelectron spectroscopy (XPS) at Photon Factory beamline 13A and x-ray absorption (XAS) and emission (XES) spectroscopy at the undulator beamline BL07LSU in SPring-8.

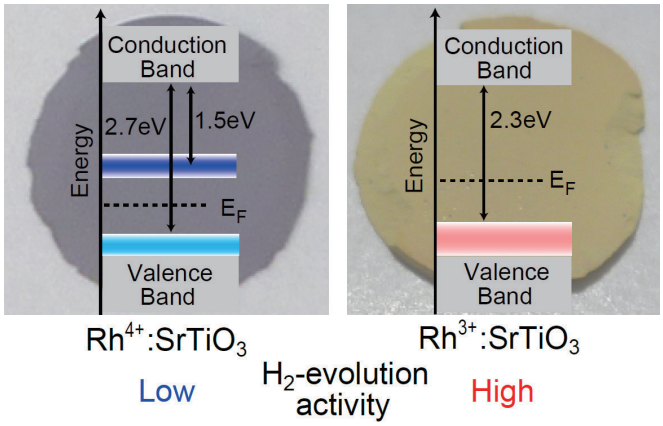

Fig. 1. Photographs of Rh^{4+}:$SrTiO_3$ and Rh^{3+}:$SrTiO_3$ pellets showing the different colors and the Rh in-gap state locations relative to the valence and conduction band edges of $SrTiO_3$. The yellow Rh^{3+}:$SrTiO_3$ is photocatalytically more efficient due to the lack of a mid-gap recombination state.

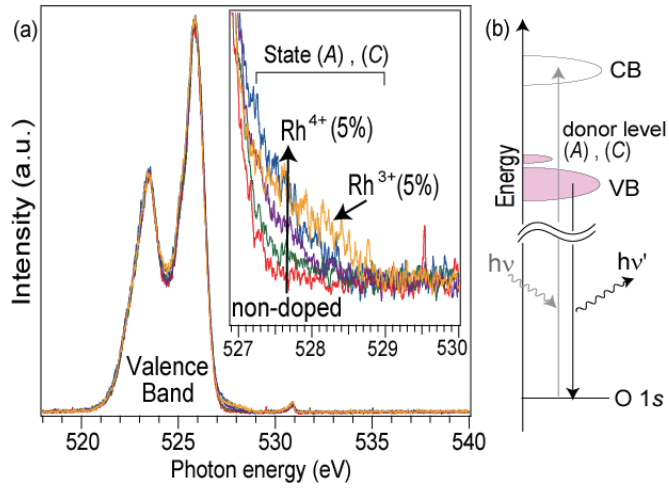

Fig. 2. (a) X-ray emission spectra of various Rh-doped $SrTiO_3$ samples showing the presence of an occupied Rh state close to the top of the valence band of $SrTiO_3$. (b) Illustration of the XES process and the location of the Rh donor levels just above the $SrTiO_3$ valence band edge.

The XPS experiments were used to investigate the violet-to-yellow color change reaction that occurs when Rh:$SrTiO_3$ is reduced, typically during the initial induction period of an electrochemical reaction. $SrTiO_3$ thin films with several different Rh doping levels were grown at various temperatures and ambient oxygen pressures. The Rh 3*d* XPS profile analysis showed that the color shift is caused by a change in the Rh impurity valence, with Rh^{4+}:$SrTiO_3$ being violet and Rh^{3+}:$SrTiO_3$ yellow [1]. Significant variations were also observed in the Rh content at the catalyst surface due to evaporative loss of Rh at high crystal growth temperatures.

A more detailed analysis of the in-gap energy levels was undertaken by XAS and XES analysis of powder samples. The XAS analysis, which probes unoccupied states, was used to show that a mid-gap unoccupied state appears only in samples containing the Rh^{4+} valence state, as illustrated in Fig. 1. Reduced Rh^{3+}:$SrTiO_3$ powders did not show a mid-gap state. Both Rh valence states lead to the appearance of an occupied impurity level close to the top of the valence band, as shown by XES spectra in Fig. 2. In addition to an increase of spectral weight with Rh doping just above the valence band top, a shift was observed in the locations of the Rh^{4+} and Rh^{3+} impurity levels. A conclusion of the analysis was that the Rh^{3+}:$SrTiO_3$ material shows higher photocatalytic activity due to the lack of a mid-gap unoccupied energy level that would lead to rapid photocarrier recombination. However, the photogenerated charge collection efficiency is limited by the lack of strong hybridization between the deep Rh levels and the O2*p* character valence band of $SrTiO_3$.

References
[1] S. Kawasaki, K. Nakatsuji, J. Yoshinobu, F. Komori, R. Takahashi, M. Lippmaa, K. Mase, and A. Kudo, Appl. Phys. Lett. **101**, 033910 (2012).
[2] S. Kawasaki, K. Akagi, K. Nakatsuji, S. Yamamoto, I. Matsuda, Y. Harada, J. Yoshinobu, F. Komori, R. Takahashi, M. Lippmaa, C. Sakai, H. Niwa, M. Oshima, K. Iwashina, and A. Kudo, J. Phys. Chem. C **116**, 24445 (2012).

Authors:
S. Kawasaki, K. Nakatsuji, S. Yamamoto, I. Matsuda, Y. Harada, J. Yoshinobu, F. Komori, R. Takahashi, M. Lippmaa, K. Akagi[a], C. Sakai[b], H. Niwa[b], M. Oshima[b], K. Mase[c], K. Iwashina[d], and A. Kudo[d].
[a]Tohoku University
[b]Department of Applied Chemistry, University of Tokyo
[c]High Energy Accelerator Research Organization
[d]Tokyo University of Science

Pressure-Induced Heavy Fermion Superconductivity in the Nonmagnetic Quadrupolar System $PrTi_2Al_{20}$

Uwatoko and Nakatsuji Groups

Unconventional superconductivity (SC) with a variety of exotic characters such as anisotropic superconducting gap, large critical field and effective mass, reentrant SC, FFLO SC, etc. has attracted much attention in condensed matter physics. Since most of these unconventional superconductors have been found near a magnetic quantum critical point (QCP), where the magnetic ordering temperature is suppressed to zero due to the Kondo effect, the interesting question is what would happen near the QCP of orbital order. Although, there have been some theoretical suggestions that orbital fluctuations play an important role in iron based superconductors, it is hard to study experimentally because orbital degree of freedom is strongly coupled with spin and charge degrees of freedom in *d*-electron compounds. In contrast, pure orbital degree of freedom sometimes appears as a quadrupole moment in *f*-electron compounds such as nonmagnetic Γ_3 state in cubic Pr or U based compounds

The cubic Γ_3 compound $PrTi_2Al_{20}$ has demonstrated the interplay of a ferroquadrupole order at T_Q = 2 K and Kondo effect through the strong *c*-*f* hybridization [1]. Furthermore, it exhibits SC at T_{SC} = 0.2 K with the associated enhanced effective mass ~16 m_0 [2]. Here we report the discovery of a pressure-induced heavy fermion superconductivity in a nonmagnetic orbital ordering system $PrTi_2Al_{20}$. In particular, we found that the transition temperature and the effective mass associated with the superconductivity are dramatically enhanced to more than 100 m_0 as the system approaches the putative quantum critical point of the orbital order [3].

Figure 1(a) shows the temperature dependence of the magnetic resistivity ρ_{mag} measured under various pressures. At high temperatures, the T_{max} due to the magnetic Kondo

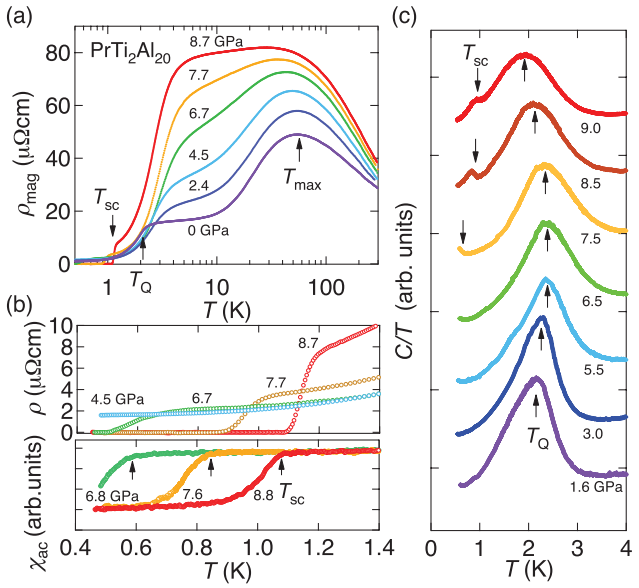

Fig. 1. (a) Magnetic part of the resistivity, ρ_{mag}, versus the logarithm of the temperature under various pressures. Here, ρ_{mag} is obtained by subtracting the resistivity of $LaTi_2Al_{20}$ obtained under ambient pressure from that of $PrTi_2Al_{20}$. (b) Temperature dependence of the resistivity and the ac magnetic susceptibility at low temperatures. A large diamagnetic signal due to the SC transition is observed at a lower temperature, which corresponds to nearly 60% superconducting shielding, estimated by comparing to the diamagnetic signal of lead with almost the same size as the sample of $PrTi_2Al_{20}$. (c) Temperature dependence of the ac specific heat divided by temperature for different pressures. The curves are shifted vertically for clarity.

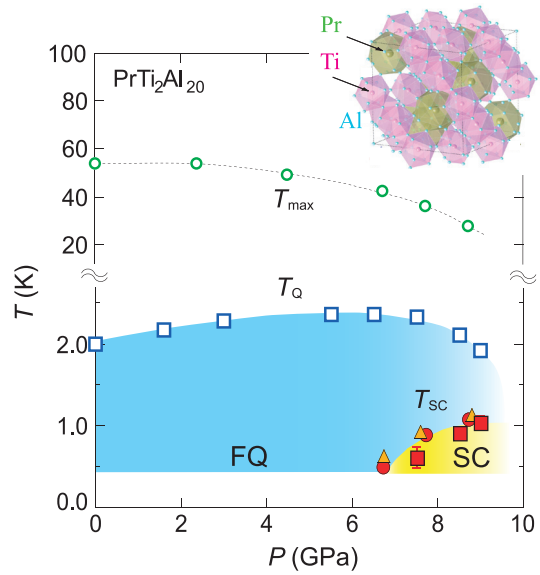

Fig. 2. Open circles and squares represent the position of T_{max} determined from the maximum in the temperature dependence of the resistivity and the ferroquadrupole ordering temperature T_Q, respectively. The SC transition temperatures T_{SC} are deduced from the temperature dependence of the resistivity (closed circles), the ac magnetic susceptibility (closed triangles), and the ac specific heat (closed squares), respectively. The inset shows the cubic crystal structure of $PrTi_2Al_{20}$. Cages made by $PrAl_{16}$ and $TiAl_{12}$ are indicated in green (larger cages) and purple (smaller cages), respectively.

effect using the excited magnetic CEF levels decreases with pressure, suggesting that pressure slightly reduces the CEF splitting. At lower temperatures, the quadrupole ordering temperature T_Q = 2K at ambient pressure can be traced as a sharp resistivity drop up to P = 4.5 GPa and shows a slight increase with pressure. Surprisingly, above 6.7 GPa, another anomaly was observed at lower temperatures. The resistivity shows an abrupt drop to zero at 0.7 K at 6.7 GPa, indicating the onset of superconductivity. With further increasing pressure, the resistivity drop becomes sharper, and temperature of zero resistance increases up to 1.1 K at P = 8.7 GPa. The observation of a large diamagnetic response in the ac magnetic susceptibility at almost the same temperature as the onset of the zero resistance state indicates that pressure-induced superconductivity is of bulk origin (Fig. 1(b)). To further elucidate the interplay between the superconductivity and ferroquadrupole order, we measured the specific heat under pressure (Fig. 1(c)). At 1.6 GPa, the specific heat divided by temperature C/T shows a peak due to the quadrupolar ordering at T_Q ~ 2 K. With increasing the pressure, T_Q monotonically goes up to P = 5.5 GPa, however, further increase of the pressure starts broadening and shifting the transition to a lower temperature and instead induces a well-defined subsequent anomaly on cooling associated with the superconducting transition. The superconducting anomaly appears at the temperature in full agreement with those found in the resistivity and ac magnetic susceptibility measurements, providing further evidence for the bulk superconductivity. Pressure-induced evolution of ferroquadrupolar and superconducting phases of $PrTi_2Al_{20}$ is summarized in the temperature-pressure phase diagram (Fig. 2). After peaking at P = 6 GPa, the ferroquadrupole ordering temperature becomes suppressed with significant broadening, indicating the presence of the associated QCP.

At 8.7 GPa, a critical magnetic field B_{c2} is estimated to be more than 3 T, which is the highest value among Pr-based heavy fermion superconductors and similar to the case found in the Ce-based heavy fermion superconductors. Our results

suggest a generic phase diagram hosting unconventional superconductivity on the border of orbital order, paving a new path for further research on novel quantum criticality and superconductivity due to orbital fluctuations.

References

[1] A. Sakai and S. Nakatsuji, J. Phys. Soc. Jpn. **80**, 063701 (2011).
[2] A. Sakai, K. Kuga, and S. Nakatsuji, J. Phys. Soc. Jpn. **81**, 083702 (2012).
[3] K. Matsubayashi, T. Tanaka, A. Sakai, S. Nakatsuji, Y. Kubo, and Y. Uwatoko, Phys. Rev. Lett. **109**, 187004 (2012).

Authors

K. Matsubayashi, A. Sakai, S. Nakatsuji, Y. Uwatoko, T. Tanaka[a], and Y. Kubo[a]

[a]Nihon University

Surface Magnetotransport in Quantum Hall Ferromagnetic Phase in the Organic Dirac Fermion System

Osada Group

In the 2D massless Dirac fermion systems with charge neutrality, the ν=0 quantum Hall (QH) state appears at the high-field quantum limit, resulting from the breaking of four-fold (spin and valley) degeneracy of the n=0 Landau level. Two kinds of ν=0 QH states appear depending on the ratio of spin splitting and valley splitting: One is the spin-unpolarized QH insulating phase, and the other is the spin-polarized QH ferromagnetic phase accompanied by the metallic edge state consisting of a pair of n=0 QH edge states with opposite spin and chirality (helical edge state). The high-field ground state is one of the key issues of the physics of the Dirac fermion system. In undoped graphene, it has been believed that the high-field ground state is the QH insulator.

On the other hand, the Q2D Dirac fermion system, in which 2D massless Dirac layers stack with weak interlayer coupling, is realized in a layered organic conductor α-(BEDT-TTF)$_2$I$_3$ under pressures P>1.5GPa. We found the experimental evidences that the high-field ground state is the QH ferromagneric phase (Fig.1(a)) in α-(BEDT-TTF)$_2$I$_3$ in contrast to graphene. In α-(BEDT-TTF)$_2$I$_3$, the interlayer

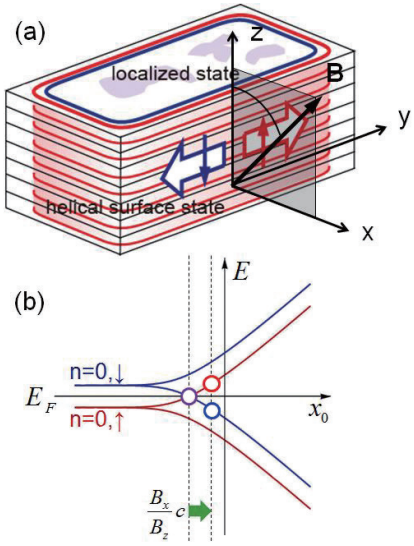

Fig. 1. (a) Helical edge state surrounding the ν=0 QH ferromagnet. (b) Edge state dispersion around the layer edge. Interlayer tunneling causes the shift of x_0.

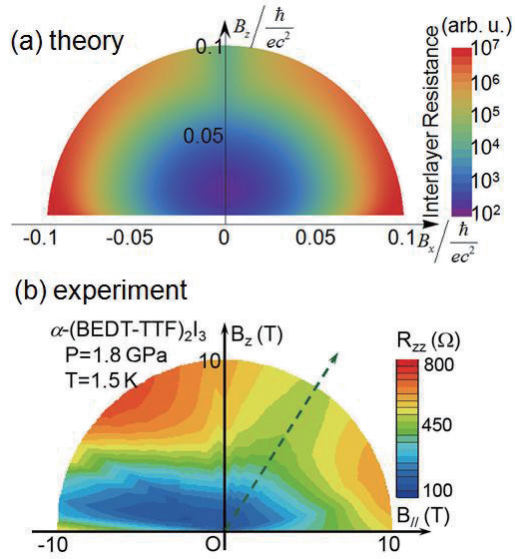

Fig. 2. Interlayer resistance as a function of strength and orientation of magnetic fields. (a) calculation. (b) experiment in α-(BEDT-TTF)$_2$I$_3$.

magnetoresistance shows anomalous saturation at high fields. The saturation resistance is scaled not by the sectional area of sample crystals but by sample perimeter. These experimental facts strongly suggest the interlayer surface transport due to the helical edge state on side surfaces of crystals. The existence of the helical edge state directly means the QH ferromagnet.

We have considered the mechanism of interlayer surface transport due to helical edge state. Since the helical edge state is not topologically protected, transport along the helical edge channel must be diffusive due to spin-inversion scattering. So, we can assume that the interlayer tunneling occurs less frequently than the scattering on the single layer edge. In this case, the interlayer surface transport is dominated by the single tunneling process between the edge states on neighboring two layers. The selection rule of this tunneling leads the shift of center coordinate x_0 under finite in-plane magnetic field B_x as shown in Fig.1(b). Therefore, the interlayer tunneling is allowed only when the magnetic field is parallel to the side surface of the crystal (B_x =0).

Figure 2(a) shows the calculated interlayer resistance R_{zz}, which includes the bulk contribution, as a function of strength and orientation of magnetic fields. We can see that R_{zz} shows the saturation when the magnetic field is swept in the vertical direction, but shows monotonous increase in other directions. Fig. 2(b) shows the measured interlayer resistance R_{zz} in α-(BEDT-TTF)$_2$I$_3$. The saturation occurs when the magnetic field was parallel to the stacking direction. Observed features are well explained by the calculation. This agreement also indicates the appearance of the QH ferromagnetic phase with the helical edge state in α-(BEDT-TTF)$_2$I$_3$.

Authors

T. Osada, M. Sato, T. Konoike, and K. Uchida

Mn^{3+}/Mn^{4+} Charge Order Driven by K-Vacancy Order in Mn-Hollandite

Y. Ueda Group

Hollandite type oxides, $K_2M_8O_{16}$ with a mixed valence of M^{3+}/M^{4+} =1/3 have intensively investigated, expecting novel itinerant properties such as metal-insulator (MI) transition, charge order and so on. Actually, $K_2V_8O_{16}$ was found to undergo the metal-insulator transition at 170K, accompanied by the structural transition and charge order [1, 2]. A very rare ferromagnetic MI transition was discovered in $K_2Cr_8O_{16}$ [3]. This MI transition is caused by a Peierls instability in the quasi-one-dimensional column structure made of four coupled Cr-O chains running in the *c*-direction, leading to the formation of tetramers of Cr ions below the transition temperature [4].

The crystal structure consists of the M_8O_{16}-framework and K-cations. The M_8O_{16}-framework is constructed from the double-chains (zigzag-chains) formed by sharing the edges of MO_6 octahedra. The M_8O_{16}-framework has rectangular tubes surrounded by four double-chains, and K-cations occupy the sites within each rectangular tube and act as electron donor.

$K_xMn_8O_{16}$ was prepared by high-pressure synthesis using a cubic anvil press [5]. Unfortunately Mn-hollandite was obtained only in K-deficient form. The maximum K-composition is x=1.6, in which K-vacancy molar fraction is 1/5 and Mn^{3+} molar fraction is also the same 1/5. $K_{1.6}Mn_8O_{16}$ is not a metal and a canted antiferromagnet with Néel temperature of 50 K. Resistivity well obeys a one-dimensional variable range hopping manner. $K_{1.6}Mn_8O_{16}$ shows successive structural transitions of tetragonal to monoclinic at 370 K and monoclinic to monoclinic at 250 K. The superlattice reflections with five-fold periodicity along the *b*-axis (tunnel direction) as shown in Fig. 1, are observed by electron diffraction of TEM (transmission electron microscope) below 250 K. Such a five-fold periodicity is consistent with the fraction of K-vacancies, 0.4/2=1/5, suggesting vacancy-ordering at 250 K. At room temperature, similar but rather diffusive super-reflections are observed. These results suggest that in $K_{1.6}Mn_8O_{16}$, the charge differentiation into Mn^{3+} and Mn^{4+} occurs even at higher temperature than at least 370 K and a short range order of K-vacancies progresses below 370 K, followed by a sudden long range order at 250 K. Such charge differentiation in $K_{1.6}Mn_8O_{16}$ could be due to K-deficiency, because the fraction of Mn^{3+} is 1/5 which coincides with the fraction of K-vacancies. Namely, extra e_g-electrons are trapped at Mn ions close to K-vacancies, giving rise to Mn^{3+} ions, namely an ordering between Mn^{3+} and Mn^{4+} takes place in cooperation with K-vacancy ordering. An origin for K-deficiency in hollandite manganese oxide could be in its rather shorter *b*-axis compared with those of $K_2M_8O_{16}$ (M = Ti, V, Cr). The electrostatic repulsion between K^+ ions in the tunnel would not allow the full occupancy of K-sites. Much higher pressure would be necessary for the synthesis of the stoichiometric $K_2Mn_8O_{16}$.

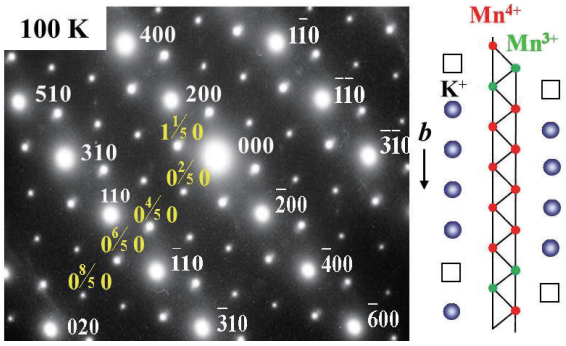

Fig. 1. Electron diffraction pattern observed at 100 K and schematic illustration of charge order between Mn^{4+} and Mn^{3+} for $K_{1.6}Mn_8O_{16}$. The electron beam incidence is along the [001] direction of the monoclinic lattice. The superlattice reflections with five-fold periodicity along the *b*-axis (tunnel direction) are clearly observed, indicating K-vacancies ordering. The extra electrons are trapped by Mn ions adjacent to K-vacancies, leading to charge order between Mn^{4+} and Mn^{3+}.

References

[1] M. Isobe, S. Koishi, N. Kouno, J. Yamaura, T. Yamauchi, H. Ueda, H. Gotou, T. Yagi, and Y. Ueda, J. Phys. Soc. Jpn. **75**, 073801 (2006).
[2] A. C. Komarek, M. Isobe, J. Hemberger, D. Meier, T. Lorenz, D. Trots, A. Cervellino, M. T. Fernández-Díaz, Y. Ueda, and M. Braden, Phys. Rev. Lett. **107**, 027201 (2011).
[3] K. Hasegawa, M. Isobe, T. Yamauchi, H. Ueda, J-I. Yamaura, H. Gotou, T. Yagi, H. Sato, and Y. Ueda, Phys. Rev. Lett. **103**, 146403 (2009).
[4] T. Toriyama. A. Nakao, H. Nakao, Y. Murakami, K. Hasegawa, M. Isobe, Y. Ueda, A. V. Ushakov, D. I. Khomskii, S. V. Streltsov, T. Konishi, and Y. Ohta, Phys. Rev. Lett. **107**, 266402 (2011).
[5] T. Kuwabara, M. Iosbe, H. Gotoh, T. Yagi, D. Nishio-Hamane, and Y. Ueda, J. Phys. Soc. Jpn. **81**, 104701 (2012).

Authors
M. Isobe, H. Gotoh, D. Nishio-Hamane, and Y. Ueda

Interlayer Switching of Reduction in Layered Bi-V Oxide

Y. Ueda Group

The pseudo binary oxide system Bi_2O_3-V_2O_5 has received considerable interest due to its wide structural diversity and rich functional properties. Of particular interest is Aurivillius phase $Bi_4V_2O_{11}$ which is found exhibiting remarkably high oxygen anionic mobility. Such a function promises serious potential applications in many important areas, *e.g.* solid oxide fuel/electrolysis cells and oxygen sensors. The crystal structure of idealized $Bi_4V_2O_{11}$ is built up from infinite $(Bi_2O_2)^{2+}$ sheets sandwiched between oxygen deficient $VO_{4-\Delta}$ perovskite slabs (V-O layer). Intrinsic oxygen vacancies (Δ = 0.5) in the V-O layer, which is normally believed to enable high oxide ion conductivity, are located in both apical and equatorial sites of VO_6 octahedra randomly. Such a description represents a

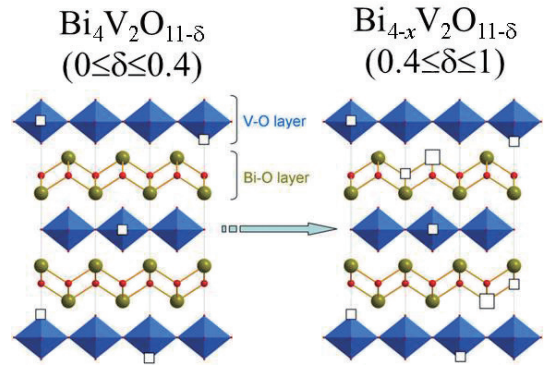

Fig. 1. Interlayer Switching of Reduction from V-O layers to Bi-O layers in Layered Oxide, $Bi_4V_2O_{11-\delta}$ ($0\leq\delta\leq1$). With increasing oxygen deficiency in $Bi_4V_2O_{11-\delta}$, the reduction of $Bi_4V_2O_{11-\delta}$ first proceeds in the V-O layers, but beyond δ=0.4, suddenly switched to the Bi-O layers by precipitation of metallic bismuth, retaining a molar ratio of V^{4+}/V^{5+} = 2/3, namely the relation between bismuth and oxygen deficiencies is expressed as $x = 2\delta/3 - 4/15$ in $Bi_{4-x}V_2O_{11-\delta}$ ($0.4\leq\delta\leq1$).

widely accepted prototype structure for the high temperature γ-phase. With decreasing temperature, $Bi_4V_2O_{11}$ undergoes two consecutive and reversible phase transitions, γ→β and β→α at 553 and 386 ºC, respectively, due to the long range oxygen vacancy ordering process.

The oxygen-vacancy-disordered γ-phase reminds us that there might exist a rich phase diagram in the oxygen deficient system where a wealth of unknown phases would be expected. Moreover, $Bi_4V_2O_{11-\delta}$ is of particular interest as the two-dimensional square lattice enables Aurivillius a favoured structure carrier of novel quantum properties. A full phase diagram for the $Bi_4V_2O_{11-\delta}$ ($0\leq\delta\leq1$) system was built for the first time by examining the whole spectrum of composition [1]. One structure (α-phase) related to the established $Bi_4V_2O_{11}$ phase survives in a very narrow δ range (≈ 0.1) whereas the other structure type (A-type) with its parent phase $Bi_4V_2O_{10.6}$ shows unusual robustness from δ=0.4 until δ=1 ($0.1<\delta<0.4$: two phase mixture). Surprisingly, the decreasing oxygen stoichiometry in this structural region is found to be accommodated not by lowering the valence of vanadium as would be expected, but instead by reducing bismuth. It means the Bi site is favored over the V site upon reduction. This conclusion was further strengthened by the measurements of magnetic susceptibility over different compositions. All samples ($0.4\leq\delta\leq1$) show the similar behavior that is characteristic of a one dimensional S = ½ antiferromagnetic Heisenberg chain model. The rigid V-O unit shared by all compositions between δ=0.4 and 1 is thus responsible for the robustness of the second type structure in the current phase diagram. *In situ* XRD investigations as a function of temperature provided strong evidence for the existence of three allotropic forms, which are α, β and γ for the $Bi_4V_2O_{11}$ type and A, B and γ for the $Bi_4V_2O_{10.6}$ type. When heated to 570ºC or higher temperature, all compositions become uniform by forming the same tetragonal γ phase.

These results means that the reduction of $Bi_4V_2O_{11-\delta}$ first proceeds in the V-O layer, but beyond δ=0.4, suddenly switched to the Bi-O layer by precipitation of metallic bismuth, retaining a molar ratio of V^{4+}/V^{5+} = 2/3, namely the relation between bismuth and oxygen deficiencies is expressed as $x = 2\delta/3 - 4/15$ in $Bi_{4-x}V_2O_{11-\delta}$ ($0.4\leq\delta\leq1$).

With a larger amount of intrinsic disordered oxygen vacancies, γ-$Bi_4V_2O_{11-\delta}$ phases, particularly γ-$Bi_{3.6}V_2O_{10}$ hold great potentials in offering optimized ionic conductivity. On the other hand, given the interesting defect chemistry and electromagnetic properties, this oxygen deficient system provides a very unique opportunity for the study at the interplay between structure and property.

Reference
[1] Y. Zhang and Y. Ueda, Inorganic Chemistry **52**, 5206 (2013).

Authors
Y. Zhang and Y. Ueda

A High-Resolution Detector Installed on a Focusing Small-Angle Neutron Scattering Spectrometer (SANS-U)

Shibayama Group

The small-angle neutron scattering (SANS) spectrometer SANS-U, owned by ISSP, is installed on the C1-2 cold neutron beamline of the research reactor (JRR-3) at the Japan Atomic Energy Agency (JAEA), Tokai, Japan. Recently, SANS-U was upgraded from a pinhole SANS (PSANS) spectrometer to a focusing SANS (FSANS) spectrometer by installation of a stack of 55 MgF_2 lenses and a high-resolution position-sensitive detector (HR-PSD)[1]. Through this upgrade, the accessible low Q-limit (Q_{min}) was expanded to the order of 10^{-4} Å^{-1}, where Q is the magnitude of the scattering vector, defined by $Q = (4\pi/\lambda)\sin\theta$ (where λ and 2θ are the wavelength and the scattering angle, respectively). Observation of a scattering profile in this Q-range by means of an FSANS requires a longer measurement time longer than that of conventional PSANS. Consequently, measurement time for FSANS experiments usually has a higher proportion of total user machine time. Therefore, it is desirable to improve the experimental efficiency of FSANS measurements. In case of cold neutrons, ZnS/^{6}LiF scintillation detectors are known for lower detection efficiency compared with the conventional ^{3}He detectors. Therefore, to improve the HR-PSD, we attempted to increase the detection efficiency of the ZnS/^{6}LiF scintillator by maintaining a high spatial resolution and a low background.

In order to increase the performance of a ZnS/^{6}LiF scintillator for high-resolution detection of cold neutrons, we determined optimum thickness of the ZnS/^{6}LiF scintillator. We also examined the chrematistics of the HR-PSD with the optimized scintillator, and performed FSANS measurements in order to compare the performances with a commercial scintillator. Figure 1 shows the HR-PSD installed inside the flight-tube of the SANS-U spectrometer. Note that the HR-PSD consists of a cross-wired position-sensitive photomultiplier tube (PSPMT) combined with a ZnS/^{6}LiF scintillator. According to the specifications of the PSPMT, the size of the effective area of the PMT and its spatial resolution are about ϕ100 mm and 0.45 mm, respectively. The HR-PSD packed in an Al vessel was mounted on an X-Z movable bench in front of the main ^{3}He-PSD. Figure 2(a) shows the total count of neutrons depending on scintillator thickness. By increasing the thickness from 0.180 to 0.433 mm, the total count increased remarkably from 1.23×10^5 to 3.18 ×

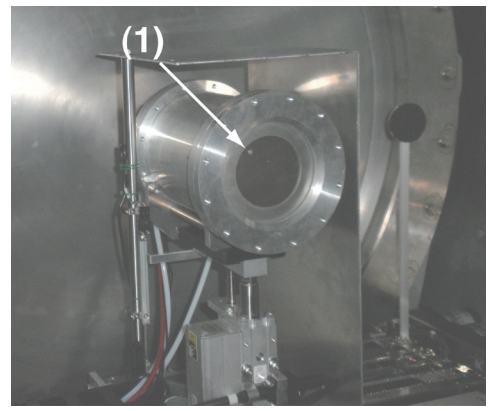

Fig. 1. Photograph of the high-resolution position sensitive detector (HR-PSD) in the flight tube of the SANS-U spectrometer. (1) The position of the fixed beam-stopper (Cd; ϕ4 mm). The details of the HR-PSD are described in another recent publication. [1]

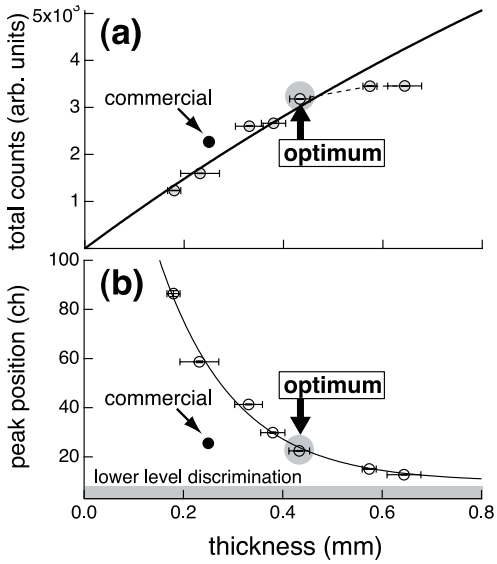

Fig. 2. Scintillator thickness dependences of (a) total count, and (b) peak position on a pulse-height spectrum for the ZnS/^{6}LiF scintillator developed by Katagiri et al. [2]

10^5. In contrast, the total count increased slightly from 3.18 × 10^5 to 3.46 × 10^5 when the scintillator thickness increased from 0.433 to 0.640 mm. Figure 2(b) shows the peak position of the pulse height spectra for varying scintillator thicknesses The peak position for a commercial scintillator was estimated to be 25.54 ch. A low peak position generally leads to a decrease in counting stability because of difficulty in electrical discrimination, whereas higher values of peak positions are suitable for count stability. Hence, a trade-off exists between the total count and peak position. On the basis of the results of the total count and peak position for varying scintillator thickness, we determined optimum thickness. The requirements for the HR-PSD were as follows: (i) high detection efficiency and (ii) peak position approximately equal to that of the commercial scintillator. Accordingly, the optimum scintillator thickness was determined to be 0.433 mm. The beam intensities obtained using the optimum ZnS/^{6}LiF scintillator were 1.39 times higher than those obtained using the commercial scintillator, which is consistent with the results of pulsed height measurements for comparison.

In conclusion, the total count of direct focused beam intensity was 1.39 times that of the commercial scintillator while maintaining both Q-resolution and the background count at the same level. This optimization resulted in a significant improvement in the experimental efficiency of the FSANS experiments.[3]

References

[1] H. Iwase, H. Endo, M. Katagiri, and M. Shibayama, M. J. Appl. Cryst. **44**, 558 (2011).
[2] M. Katagiri, K. Sakasai, M. Matsubayashi, T. Nakamura, Y. Kondo, Y. Chujo, H. Nanto, and T. Kojima, Nucl. Instrum. Methods A **529**, 274 (2004).
[3] H. Iwase, M. Katagiri, and M. Shibayama, M. J. Appl. Cryst. **45**, 507 (2012).

Authors

H. Iwase, M. Katagiri[a], and M. Shibayama
[a]Japan Atomic Energy Agency

Glass Transition of Hydrogen Atoms in Palladium Lattice

Yamamuro Group

Palladium hydride (PdH_x) is the most popular metal hydride which has been investigated by many physicists and chemists. It has been remarked also from industrial points of view, *e.g.*, hydrogen storage, filters, sensors, catalysts, etc. Figure 1 shows the adsorption isotherm of the Pd and hydrogen gas system [1]. On adsorption, a hydrogen molecule (H_2) dissociates into two hydrogen atoms (2H). It is known that the α phase appears in a lower concentration (x) region while the β phase in a higher x region. In the intermediate region (dome-like area of Fig. 1), the α and β phases coexist and pressure becomes constant according to the Gibbs phase rule. Above the critical point (2.0 MPa, 259ºC), one cannot distinguish the α and β phases. Both α and β phases have an fcc structure. Most of the H atoms are located at the octahedral sites in the β phase, while the positions of the H atoms are not known in the α phase. The volume of the β phase is 11% larger than that of the α phase. There are still many unsolved interesting problems in PdH_x, *e.g.*, superconductivity at a higher x region, a surface ferromagnetic phenomenon, etc. The present work is associated with a mysterious phenomenon called "50 K anomaly". We have measured the heat capacity of the β phase with various x using an adiabatic calorimeter which was modified for *in situ* introduction of hydrogen gas into the sample cell.

Figure 2 shows the heat capacities of PdH_x (x = 0.638, 0.725, 0.782, 0.829). For all of the samples, a heat capacity anomaly appeared around 50 K as expected from the previous work [2, 3]. We have fitted the data at temperatures lower than the anomaly to the function,

$$C_p = C(\text{Debye}) + C(\text{Einstein}) + \gamma T, \qquad (1)$$

where the first and second terms correspond to the acoustic and optical vibrations, respectively and the third term represents the electronic heat capacity. It was revealed that C(Einstein) does not contribute in this temperature range since the mass of an H atom is much smaller than that of a Pd atom. The coefficient γ was determined not by the fitting but by the interpolation for the previous heat capacity data at very low temperatures [4]. The fitting was satisfactory for all samples as shown in Fig. 2. The Debye temperature θ_D determined by the fitting is 246 K, being mostly independent from x in the β phase. This value is smaller than that of pure Pd (θ_D = 276 K), meaning that the Pd lattice is

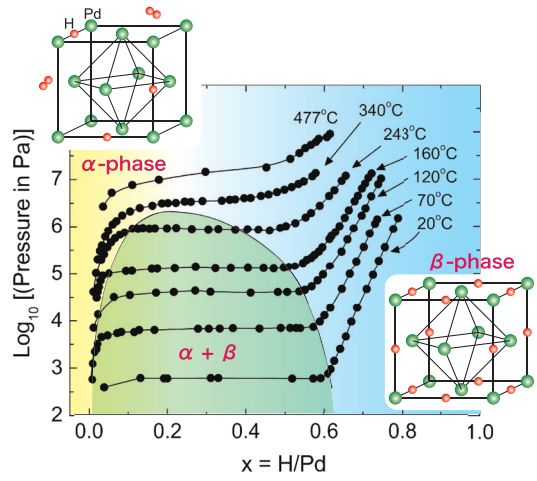

Fig. 1. Adsorption isotherms of Pd-H system and schematic structure of the α and β phases of PdH_x.

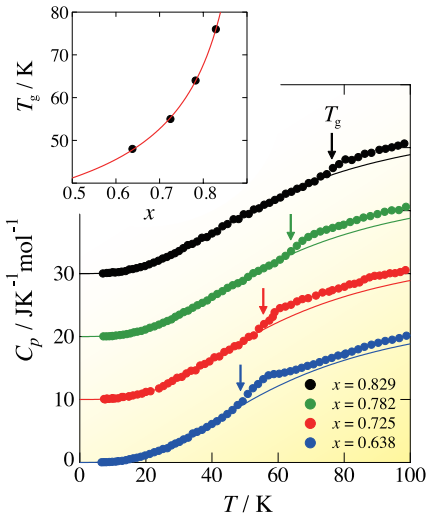

Fig. 2. Heat capacities of PdH_x (x = 0.638, 0.725, 0.782, 0.829). The arrows represent the glass transition temperatures T_gs whose x dependence is shown in the inset. The curves in the C_p and T_g figures represent the results of the fittings to Eqs. (1) and (2), respectively. See text for the details.

softened by accommodating H atoms. In the previous studies [2, 3], the 50 K anomaly was treated as a C_p peak. From the precise analysis, however, it was found that this is a step-like anomaly. We also found that an exothermic, followed by endothermic, phenomenon appeared around the anomaly. Taking its temperature dependence and annealing effect into consideration, we conclude that the 50 K anomaly of PdH_x is not a phase transition but a glass transition that is a freezing phenomenon of the H atoms positionally disordered among the octahedral sites. This conclusion is supported by the previous NMR [5], mechanical [6], thermal relaxation [7] studies which show that the relaxation time of the jump motion of the H atoms reaches 1000 s (the time-scale of the glass transition) around 50 K.

Figure 2 demonstrates that the glass transition temperature T_g strongly depends on x. By assuming that the jump rate of the H atoms is proportional to the number of vacant sites and the Arrhenius relation is valid in this region, we derived the following equation,

$$T_g = \Delta E/[\ln(1 - x) + A]. \qquad (2)$$

where ΔE is the activation energy and A is a constant. The x dependence of T_g is reproduced well as shown the inset of Fig. 2.

We are now planning to measure the heat capacity of the PdD_x sample with expectation of isotope effects on the 50 K anomaly. It is possible to observe an ordering transition of the D atoms since the previous neutron diffraction works using PdD_x samples suggest some sort of ordering of the D atoms below 50 K.

References

[1] F. D. Manchester, Phase Diagrams of Binary Hydrogen Alloys, p.158 (2000).
[2] D. M. Nace and G. J. Aston, J. Am. Chem. Soc. **79**, 3627 (1957).
[3] H. Araki, M. Nakamura, S. Harada, T. Obata, N. Mikhin, V. Syvokon, and M. Kubota, J. Low Temp. Phys. **134**, 1145 (2004).
[4] C. A. Mackliet and A. I. Schindler, Phys. Rev. **146**, 463 (1966).
[5] D. A. Cornell and E. F. W. Seymour, J. Less-Common Met. **39**, 43 (1975).
[6] J. K. Jacobs, C. R. Brown, V. S. Pavlov, and F. D. Manchester, J. Phys. F: Metal Phys. **6**, 2219 (1976).
[7] J. K. Jacobs and F. D. Manchester, J. Phys. F: Metal Phys. **7**, 23 (1977).

Authors

H. Akiba, M. Kofu, H. Kobayashi[a], H. Kitagawa[a], and O. Yamamuro
[a]Kyoto University

Spin Nematic Interaction in Square-Lattice Antiferromagnet $Ba_2CoGe_2O_7$

Masuda Group

The interaction between magnetic moments has been well known even before the establishment of quantum dynamics and the pioneering research on various types of the magnetic correlations by P. Curie is the basis of modern magnetism. Recently the correlation of the higher order of the spin operator has attracted theoretical interest in terms of hidden order in spin disordered state [1] but the direct experimental probe to identify the correlation is absent. Meanwhile in multiferroic compound that exhibits spontaneous order both in magnetism and dielectricity, the electric polarization is expressed by second order tenors of the spin operators [2], and the spin nematic operator comes to visible. In this fiscal year we demonstrate the existence of the spin nematic interaction in an easy-plane type antiferromagnet $Ba_2CoGe_2O_7$ [3, 4] by exploring the magnetic anisotropy and spin dynamics. Combination of neutron scattering and magnetization measurements reveals that the dominant origin of the observed in-plane anisotropy is the ferro-type interaction of spin nematic operator instead of conventional single-ion anisotropy. The structure of the spontaneous polarization [10] is consistent with the ferro-type order of the nematic operators. The introduction of the spin nematic interaction is useful to understand the physics of spin and electric dipole in multiferroic compounds.

The crystal structure of $Ba_2CoGe_2O_7$ is schematized in Fig. 1**a**. The compound exhibits antiferromagnetic transition at T_N=6.7 K and a staggered antiferromagnetic structure in the (001) plane was identified [3]. Below T_N, a ferroelectric polarization is simultaneously induced [4]. Inelastic neutron scattering spectrum and magnetization measurements are shown in Figs. 1**c** and **d**, respectively. In the former clear anisotropy gap of about 0.12 meV is observed at the antiferromagnetic zone center Q = (100). In the derivative of magnetization curve, a peak due to spin flop is observed at

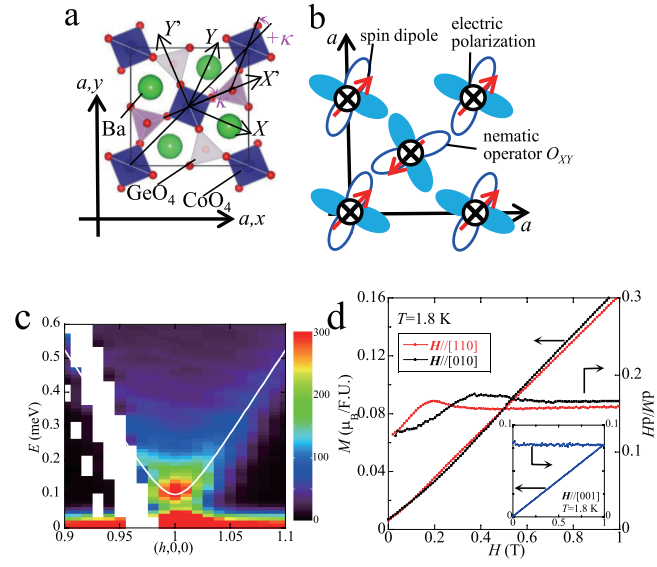

Fig. 1. **a**, Crystal structure of $Ba_2CoGe_2O_7$. **b**, Structures of spin dipoles, spin nematic operator O_{XY} , and electric polarizations in $Ba_2CoGe_2O_7$. Red arrows are spin dipoles and open circles with crosses and small filled circles indicate the directions of electric polarization calculated by using the relation between spin nematic operator and electric polarization. Two-tone clovers are nematic operators. **c**, Inelastic neutron scattering spectrum. **d**, Bulk magnetization M and the derivative by field dM/dH in field along [110], [010], and [001] at T = 1.8 K.

the field H ~ 0.2 T in H // [110], the spin flop field increases in H // [100], and no spin flop is observed in H // [001]. The results mean that the magnetic easy axis is along the [110] direction. Meanwhile, the point symmetry of CoO_4 tetrahedron, D_{2d}, does not allow the magnetic anisotropy along ⟨110⟩ as far as single ion anisotropy and two-spin exchange anisotropy are considered. Thus the anisotropy is ascribed to the interaction of higher order of spin operator. Symmetry consideration leads to the relation between the electric polarization and the spin nematic operator, $P^X = -K_{ab}O_{YZ}$, $P^Y = -K_{ab}O_{ZX}$, and $P^Z = -K_cO_{XY}$, , where X, Y, and Z are the local coordinates on CoO_4 tetrahedron as shown in Fig. 1**a**. Among these O_{YZ} and O_{ZX} are irrelevant to the anisotropy since the Z component of spin dipole is zero in the spin structure [3]. Hence we consider the nematic Hamiltonian $H_p = -J_pK_c^2\sum_{i,j} O_{XY}(i)O_{XY}(j)$. Calculation of the classical energy including antiferromagnetic spin interaction and ferro-type nematic interaction between O_{XY} operators leads the ground state to the staggered spin structure along ⟨110⟩ direction. The ferro-type nematic correlation depicted in Fig. 1**b** is consistent with the ferroelectric polarization along Z direction previously reported [4]. Both neutron spectrum and bulk magnetization are quantitatively explained by extended spin-wave calculation based on Hamiltonian including the ferro-type nematic interaction.

References

[1] A. F. Andreev and I. A. Grishchuk, Sov. Phys. JETP **60**, 267 (2984).
[2] H. Katsura, N. Nagaosa, and A.V. Balatsky, Phys. Rev. Lett. **95**, 057205 (2005).
[3] A. Zheludev *et al.*, B. Phys. Rev. B **68**, 024428 (2003).
[4] H. Murakawa *et al.*, Y. Phys. Rev. Lett. **105**, 137202 (2010).

Authors

M. Soda, T. Masuda, M. Matsumoto[a], M. Mansson[b], S. Ohira-Kawamura[c], and K. Nakajima[c]
[a]The Shizuoka University
[b]Tokyo Paul Sherrer Institute
[c]J-PARC

---International MegaGauss Science Laboratory------

Determination of Entropies by Measurements of Magneto-Caloric Effects in Pulsed Magnetic Fields

Tokunaga and Katsumoto Groups

Existence of highly degenerated ground states, *e.g.* in frustrated magnets, results in the emergence of various non-trivial physical phenomena. Such degeneracy involves significant residual entropy at low temperatures, whereas its direct determination is not easily achieved. Our measurement system of the magneto-caloric effects (MCEs) in pulsed high magnetic fields provides unique opportunity to study the residual entropies. Fast field-sweep rates in the pulsed fields enable us to realize effectively adiabatic conditions in the magnetization processes, and hence, accurate evaluation of the entropies in wide range of magnetic fields up to 55 T.

With using our system, we measured the MCEs in $Gd_3Ga_5O_{12}$ (GGG) [1], which does not show long-range order of Gd moments down to 25 mK owing to geometrical spin frustration. Through the measurements of magnetoresistance in calibrated resistive film thermometers grown on top of the sample surfaces, we successfully monitored the instantaneous change in the sample temperature in duration of the pulsed fields (~ 36 ms). The solid lines in Fig. 1 show the field dependence of the temperature of GGG. The reversible profiles indicate that the heat exchange to the thermal bath and the delay in the response of the thermometer are negligibly small. In addition, the present results show reasonable agreement with the preceding results [2] (open circles) indicating the quantitative validity of the present system.

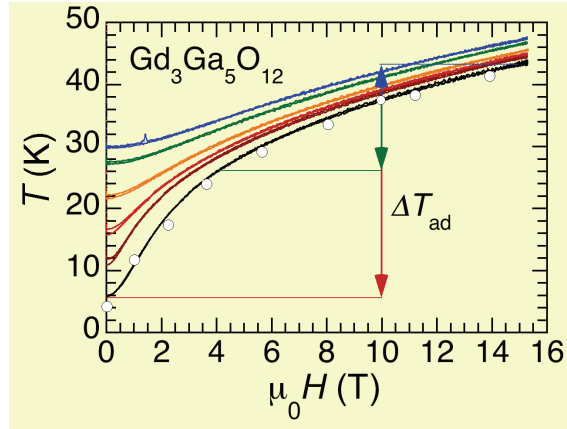

Fig. 1. Magnetic field dependence of the temperature of $Gd_3Ga_5O_{12}$ measured in pulsed magnetic fields. Open circles represent the reported results derived from the analyses of the magnetization curve measured in the quasi-adiabatic condition [2]. The inset shows a schematic illustration of the film thermometer grown on the sample.

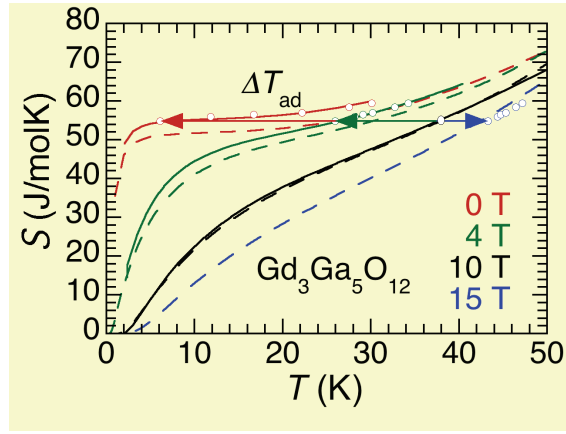

Fig. 2. Temperature dependence of the entropy of $Gd_3Ga_5O_{12}$ at several magnetic fields. The open circles were determined by the horizontal shift of the standard S-T curve at 10 T by the amount of ΔT_{ad} in the measurements of the MCEs. The solid lines were evaluated by numerical integration of the heat capacity data at various fields. The dashed lines are calculated S-T curves based on a simple crystal field model [3].

From these data, we can evaluate the entropy (S) as a function of temperature (T) for various fields. First, we determined the standard S-T curve by integrating the data of specific heat (C) at 10 T, where the residual entropy seems to be negligible at the lowest temperature for the specific heat measurement (2 K). Then the S-T curves at different fields (open circles) were determined by horizontal shift by ΔT_{ad} determined by measurements of MCEs as shown by the arrows in Figs. 1 and 2. The solid lines in Fig. 2 are the S-T curves evaluated by numerical integration of the specific heat data, in which the amounts of the residual entropies, i.e. the vertical offsets, were determined so as to match with the MCE results. The result reveals the failure of the simple estimation of the entropy by a simple crystal field model (dashed lines), while this discrepancy cannot be resolved by the C-T curves in this temperature range.

References

[1] T. Kihara *et al*, submitted to Rev. Sci. Instrum.
[2] R. Z. Levitin *et al*, J. Magn. Magn. Mater. **170**, 223 (1997).
[3] W. Dai, E. Gmelin, and R. Kremer, J. Phys. D: Appl. Phys. **21**, 628 (1988).

Authors
T. Kihara, Y. Kohama, Y. Hashimoto, S. Katsumoto, and M. Tokunaga

---Laser and Synchrotron Research Center/ Synchrotron Radiation Laboratory----------

Exotic spin states in $SrCu_2(BO_3)_2$ at Megagauss Magnetic Fields

Y. Matsuda and Takeyama Groups

Quantum spin frustration induces interesting magnetic states in matters. A orthogonal dimer spin system $SrCu_2(BO_3)_2$ exhibits fascinating phenomena due to the frustration [1]. The crystal lattice is topologically equivalent to the Shastry-Sutherland (SS) lattice. The nearest neighbor (*NN*) S=1/2 spins of Cu ions are antiferromagnetically coupled and form the singlet dimer through the exchange interaction J. Since the inter dimer exchange interaction J' between the next nearest neighbor (*NNN*) Cu ions is antiferromagnetic as well, the orthogonal configuration makes the quantum frustration. The multiple magnetization plateaux found in high magnetic fields have attracted significant attention as the exotic phenomena. [1, 2] The distinct 1/8, 1/4, and 1/3 plateaux were observed in the magnetization process and the existence of the long predicted 1/2 plateau was reported by the magnetostriction measurement [3]. However, the whole 1/2 plateau phase was not unveiled yet because of the technical upper limit of the magnetic field 100 T. Moreover, high-field spin states in the SS lattice are theoretically suggested to exhibit the exotic states such as the supersolid state between the 1/3 and 1/2 plateaux and that above the 1/2 plateau [4]. The quantum spin state when the density of the triplet state becomes high in the SS lattice has never been uncovered yet.

In the present work, we have investigated the spin states of $SrCu_2(BO_3)_2$ by the magnetization measurement up to 109 T using the single-turn coil method. The distinct 1/2 magnetization plateau phase has been observed in the field range from 84 to 108 T. A sharp magnetization increase at the end of the 1/2 plateau suggests the possible phase transition to the supersolid phase.

Figure 1 shows the magnetization (M) and the magnetic field derivative of the magnetization (dM/dH) as a function of magnetic field. Distinct peak structures are observed in the dM/dH curve, indicating the stepwise increase in the magnetization at critical magnetic fields (H_{cn}, n=1~6). By comparison with the magnetization curve in the previous report [2], H_{c1}~ H_{c3} correspond to the boundaries of 1/8, 1/4 and 1/3 plateaux phase. The broad double-peak structure comprised of H_{c4} and H_{c5} may suggest that there is an exotic phase between the 1/3 and 1/2 plateau phase. H_{c5} and H_{c6} clarify the whole region of 1/2 plateau. The finite slope observed at the 1/2 plateau phase can be caused by the thermal excitation. The exotic spin states in the SS lattice will be clarified with a help of detailed theoretical calculations. Such collaboration work is now in progress.

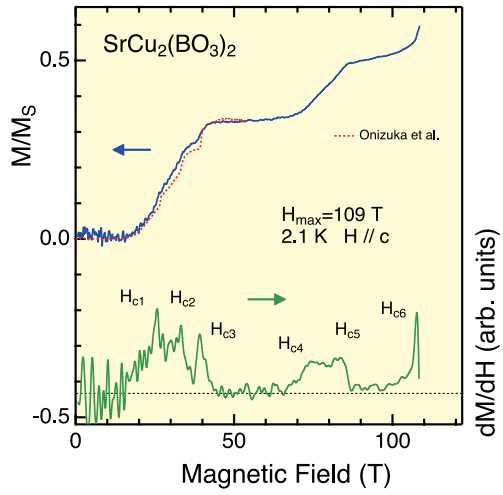

Fig. 1. A magnetization curve at 2.1 K up to 109 T. Applied field is parallel to the c-axis of the crystal. The magnetic field derivative of the magnetization (dM/dH) curve is also shown as a function of magnetic field. The dotted curve is the magnetization curve reported previously. (Ref.[2])

References
[1] H. Kageyama, K. Yoshimura, R. Stern, N. Mushnikov,K. Onizuka, M. Kato, K. Kosuge, C. Slichter, T. Goto, and Y. Ueda, Phys. Rev. Lett. **82**, 3168 (1999).
[2] K. Onizuka, H. Kageyama, Y. Narumi, K. Kindo, Y. Ueda, and T. Goto, J. Phys. Soc. Jpn. **69**, 1016 (2000).
[3] M. Jaime, R. Daou, S. A. Crooker, F. Weickert, A. Uchida, A. E. Feiguine, C. D. Batista, H. A.Dabkowska, and B. D. Gaulin, PNAS **109**, 12404 (2012).
[4] J. Lou, T. Suzuki, K. Harada, and N. Kawashima, arXiv:1212.1999v1 (2012).

Authors
Y. H. Matsuda, N. Abe, S. Takeyama, and H. Kageyama[a]
[a]Kyoto University

Terahertz Time Domain Observation of Rotational Type Spin Reorientation Transition

Suemoto Group

Ultrafast coherent excitation of spins is one of the promising technologies for developments in spintronics and information processing. Such ultrafast control of the spin systems are often studied with pump and probe measurement using femtosecond visible laser [1]. Because these methods use indirect excitations of the spins that occur as a result of dielectric interaction with optical pulses, quite large amount of optical energy, typically 10 microjoule per pulse is required for pumping the spins. For this reason, unwanted electronic excitation and heating occurs. Instead, by using the terahertz pulses, spin precession motion can be excited directly through magnetic interaction between the terahertz magnetic component and the spin system [2, 3]. As described in Fig. 1, magnetic field component of the THz pulse instantaneously tilts the spins from their equilibrium orientation,

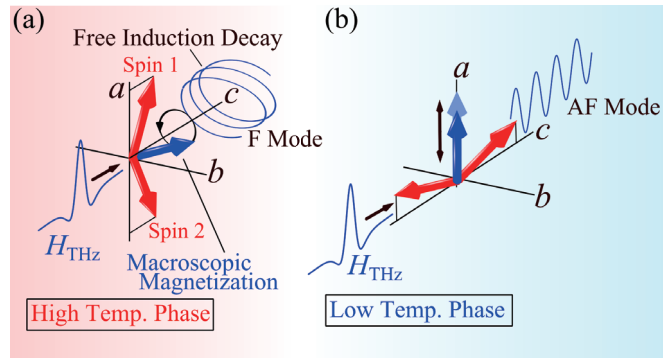

Fig. 1. Illustration of ultrafast spin precession excitation with the magnetic field component of THz pulse parallel to the a-axis for (a) high temperature phase of $ErFeO_3$, and (b) low temperature phase. In the high temperature phase, elliptically polarized emission from F mode resonance is observed. On the other hand, linearly polarized AF mode emission is observed in the low temperature phase. For the ease to see, the precessions of the individual Fe^{3+} spins 1 and 2 (red arrows) are omitted from the figures.

causing the spins to precess around the effective magnetic field. Such motion of spins emits radiation which can be observed as free induction decay signal. With this technique, spin precession can be excited and observed simultaneously with a femtojoule terahertz pulse, which enables us to ignore the heating effect. In addition, owing to the low photon energy of the terahertz pulse, unwanted electronic excitation can be avoided.

Weak ferromagnet $ErFeO_3$, which belongs to the rare earth orthoferrites known to have two magnetic resonance modes (Ferromagnetic mode and Antiferromagnetic mode) in sub-THz region [3], shows temperature induced spin reorientation transition. In this phase transition, the easy axis of the Fe^{3+} spins show 90 degree rotation. In the temperature range higher than 96 K (high temperature phase), the Fe^{3+} spins align antiferromagnetically toward the *a*-axis with a *c*-axis parallel macroscopic magnetization resulting from the canting of the spins (Fig. 1 (a)). At 87 K or lower (low temperature phase), the easy axis of the Fe^{3+} spins and the magnetization become parallel to the *c*-axis and *a*-axis, respectively (Fig. 1(b)).

Here, by focusing on the two magnetic resonance modes, we devised methods to observe the spin reorientation through THz time domain spectroscopy (TDS) and demonstrated this method with $ErFeO_3$ [4]. The measurement was performed with a sintered pellet sample and a single crystal with a (001) surface. The temperature dependence of the two resonant frequencies is shown in Fig. 2(a). It shows that the F mode frequency drops significantly around the reorientation temperature. The spectra of radiation emitted from the spin precession excited with THz magnetic field parallel to *a*-axis shows that the frequency of the emission changes significantly between high temperature phase and low temperature phase (Fig. 2(b)). Comparing this with Fig. 2(a), it can be seen that the resonant frequency equals to F mode frequency for 250 K and AF mode for 70 K. Such switching of the excited mode can be explained by rotation of the easy axis due to the spin reorientation (Figs. 1(a) and (b)) and therefore, we have shown that spin reorientation can be detected through THz TDS measurement. To the best of our knowledge, this is the first observation of such phase transitions with THz time domain measurement. When observing this behavior in the temporal waveforms, half-cycle of the precession is sufficient for distinguishing F and AF modes. Thus, by focusing on the existence of the AF mode, the phase of the spin configuration can be determined with a resolution of 0.67 ps. Therefore, this method offers ability to detect spin reorientation with picosecond time resolution and it is expected to open the doorway for studying dynamics of ultrafast spin reorientation.

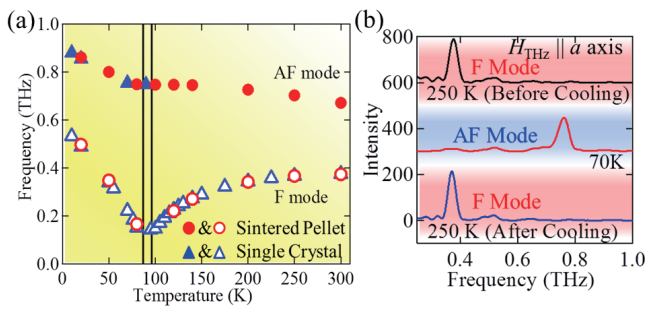

Fig. 2. (a) Temperature dependence of F and AF mode resonant frequencies in $ErFeO_3$. Circle markers show frequencies obtained with the sintered pellet, and triangle markers show frequencies in a single crystal sample with (001) surface. Two vertical lines indicate higher and lower transition temperatures at 96 K and 87 K. (b) Intensity spectra of oscillatory components obtained with $H_{THz} \parallel a$-axis THz pulse excitation.

References

[1] A. Kirilyuk, A. V. Kimel, and T. Rasing, Rev. Mod. Phys. **82**, 2731 (2010).
[2] M. Nakajima, A. Namai, S. Ohkoshi, and T. Suemoto, Opt. Exp. **18**, 18260 (2010).
[3] K. Yamaguchi, M. Nakajima, and T. Suemoto, Phys. Rev. Lett. **105**, 237201 (2010).
[4] K. Yamaguchi, T. Kurihara, Y. Minami, M. Nakajima, and T. Suemoto, Phys. Rev. Lett. **110**, 137204 (2013).

Authors

K. Yamaguchi, T. Kurihara, Y. Minami, M. Nakajima, and T. Suemoto

Firefly Bioluminescence Affected by Temperatures and Metal Ions

Akiyama Group

Firefly bioluminescence has attracted great interest among various research fields. The mechanisms of very high quantum yield and condition-sensitive color change of the bioluminescence are long standing issues of basic biochemistry and biophysics, and applications of the bioluminescence such as food hygiene inspection, DNA sequencing, bioimaging, cancer diagnosis, and immunoassay, are under intensive developments and some of them are commercially available. Quantitative study of the bioluminescence is crucially important for both basic research and application, but still very rare [1, 2].

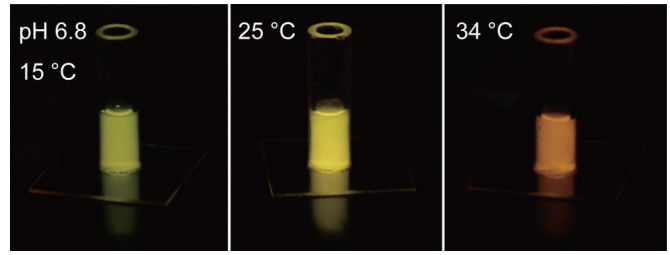

Fig. 1. Picture of temperature-sensitive color change of bioluminescence of North-American Firefly (*Photinus pyralis*) at pH 6.8 in home-made acrylate tube cell placed on an aluminum sheet.

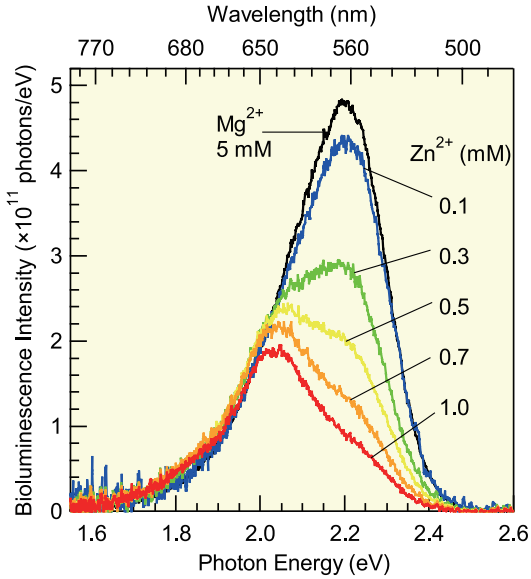

Fig. 2.Time-integrated total photon flux spectra of bioluminescence of North-American Firefly with various zinc-ion densities. Black line shows data with magnesium ion, whose density did not changed the spectra significantly, as a reference.

We measured total-photon flux of firefly bioluminescence in various reaction conditions such as temperature, pH, and bivalent metal density quantitatively. All quantitative spectra were very well reproduced by three Gaussian components, which peaked at 1.9 (red), 2.0 (orange), and 2.2 (green) eV. The positions and widths of the components were insensitive to reaction conditions. Firefly bioluminescence changed its color from yellow-green to yellow, then to orange with increasing temperature as shown in Fig. 1. Quantitative analysis revealed that the color change solely owing to decrease of intensity of the green Gaussian component with increasing temperature. Very similar color change was observed with increasing bivalent metal ion density as shown in Fig. 2. The observed similarity of color change is useful for detailed basic study such as comparisons with quantum-chemistry calculations and the robustness of the luminescence below 2.0 eV can be advantageous as a standard yield for future applications of quantitative measurement of bioluminescence.

References

[1] Y. Ando *et al*., Nature Photonics. **2**, 44 (2008).
[2] Y. Wang *et al*., Photochemistry and Photobiology **87**, 846 (2011).

Authors

T. Mochizuki, Y. Wang[a], M. Hiyama, H. Akiyama, H. Kubota[b], K. Terakado[c], T. Nakatsu[c]
[a]Chinese Academy of Science, China
[b]ATTO Corporation
[c]Kyoto University

Direct Short-Pulse Generation from Gain-Switched Semiconductor Lasers

Akiyama Group

The compact, inexpensive, and easy-to-operate gain-switched semiconductor lasers have wide potential applications as pulse light sources in industries and medical treatments [1]. However, it was very difficult to obtain short pulses with duration shorter than 10 ps through gain-switching technique. We investigated gain-switching dynamics in various semiconductor lasers [2-4], and successfully achieved Fourier-transform limited picosecond optical pulses via spectral filtering technique from gain-switched semiconductor lasers [5, 6].

Excitation-power-dependent lasing spectra from a gain-switched distributed feedback (DFB) laser diode (LD) driven by pulsed current injection with duration of nanosecond are shown in Fig. 1(a). The spectral broadening as well as the down chirping (shown as the dashed line in Fig. 1(a)) on short wavelength side are typical phenomena reflecting the large variation of carrier density during pulse generation by gain switching [6], which in turn is an important reason that results in the broadening of the gain-switched output pulses. By utilizing spectral filtering technique to extract the transient short wavelength components (Fig. 1(b)) in the lasing spectra, we have successfully generated Fourier-transform limited 4.7-ps short pulses (Fig. 1(c)) from a gain-switched DFB-LD. The present technique provides a simple and practical method for short pulse generation and brings new insights for ultrafast nonlinear dynamics producing picosecond optical pulses by gain switching.

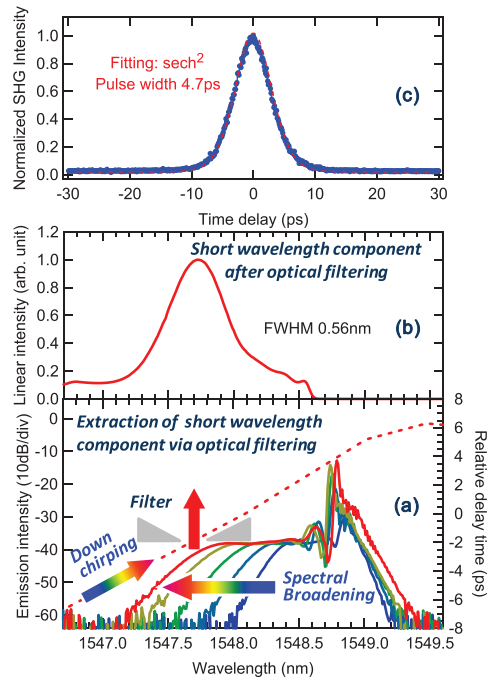

Fig. 1. (a) Lasing spectra of a single-mode DFB-LD at room temperature with various current densities, showing the significant spectral broadening towards short wavelength side with increasing current density. Dashed line shows the down chirp during gain switching of the DFB-LD with the highest excitation density. (b) Spectrum of the short wavelength component after spectral filtering of the one with the highest excitation in (a). The FWHM of the peak is measured to be 0.56 nm. (c) The autocorrelation trace of the spectrally filtered short wavelength component. Fitting result shows that the pulse has a sech^2 shape with a pulse width of 4.7 ps. The time-bandwidth product (0.33) of the obtained short pulse demonstrates that the obtained short pulses at short-wavelength side are Fourier-transform-limited pulses.

References

[1] H. Yokoyama, *et al*., Opt. Express **14**, 3467 (2006).
[2] S. Q. Chen, *et al*., Jpn. J. Appl. Phys. **51**, 098001 (2012).
[3] S. Q. Chen, *et al*., Appl. Phys. Lett. **101**, 191108 (2012).
[4] S. Q. Chen, *et al*., Opt. Express **21**, 7570 (2013).
[5] S. Q. Chen, *et al*., Opt. Express **20**, 24843 (2012).
[6] S. Q. Chen, *et al*., Opt. Express **21**, 10597 (2013).

Authors

S. Q. Chen, M. Yoshita, T. Ito, T. Mochizuki, C. Kim, H. Akiyama, A. Sato[a], and H, Yokoyama[a]
[a]Tohoku University